An updated Lagrangian LBM-DEM-FEM coupling model for dual-permeability fissured porous media with embedded discontinuities

Kun Wang · WaiChing Sun

Abstract Many engineering applications and geological processes involve embedded discontinuities in porous media across multiple length scales (e.g. rock joints, grain boundaries, deformation bands and faults). Understanding the multiscale path-dependent hydro-mechanical responses of these interfaces across length scales is of ultimate importance for applications such as CO_2 sequestration, hydraulic fracture and earthquake rupture dynamics. While there exist mathematical frameworks such as extended finite element and assumed strain to replicate the kinematics of the interfaces, modeling the cyclic hydro-mechanical constitutive responses of the interfaces remains a difficult task. This paper presents a semi-data-driven multiscale approach that obtains both the traction-separation law and the aperture-porosity-permeability relation from micro-mechanical simulations performed on representative elementary volumes in the finite deformation range. To speed up the multiscale simulations, the incremental constitutive updates of the mechanical responses are obtained from discrete element simulations at the representative elementary volume whereas the hydraulic responses are generated from a neural network trained with data from lattice Boltzmann simulations. These responses are then linked to a macroscopic dual-permeability model. This approach allows one to bypass the need of deriving multi-physical phenomenological laws for complex loading paths. More importantly, it enables the capturing of the evolving anisotropy of the permeabilities of the macro- and micro-pores. A set of numerical experiments are used to demonstrate the robustness of the proposed model.

Keywords discrete-continuum coupling, strong discontinuity, machine learning, LBM-DEM-FEM, dual-permeability, fractured porous media

1 Introduction

The geological complexity of many geo-systems, such as fractured reservoirs and faults often makes the single-permeability Darcian model inadequate to replicate the complex hydraulic behaviors [Gong et al., 2008]. This complexity is linked to the wide spectrum of pore sizes. The pores among particles, inside individual grains and crystalline planes and those formed by the dissolution and cavities are often of orders of difference in sizes. In the idealized cases where pore space distribution of a porous medium is, roughly speaking, bi-modal (e.g. fractured reservoir composed of sandstone) a dual-porosity dual-permeability model can be used to approximate the hydraulic behavior [Gerke and Genuchten, 1993, Pride and Berryman, 2003, Kuhlman et al., 2015, Borja and Choo, 2016, Choo et al., 2016]. For a fissured porous medium exhibiting a major fault, the fissures and the fault can be considered as macropores, while the pores in the intact solid matrix are considered as the micropores (Figure. 1). Then the macroscopic flow in this double porosity medium is the overlapping of both flows inside the individual systems of macropores and

Corresponding author: WaiChing Sun

Assistant Professor, Department of Civil Engineering and Engineering Mechanics, Columbia University , 614 SW Mudd, Mail Code: 4709, New York, NY 10027 Tel.: 212-851-4371, Fax: 212-854-6267, E-mail: wsun@columbia.edu

micropores, as well as the fluid transfer between the two systems of pores. Should mechanical forces or perturbations in pore pressure field take place, the major fault which is previously stable is put at the risk of being reactivated. The evolution of the microstructure of the fault results in the change of the effective macropore permeability and hence the fluid flow in macropores.

1. REV of micropores and the net of fissures, with two-dimensional periodicity

2. REV of a major fault and its neighborhood (micropores and the net of fissures), with one-dimensional periodicity along the fault
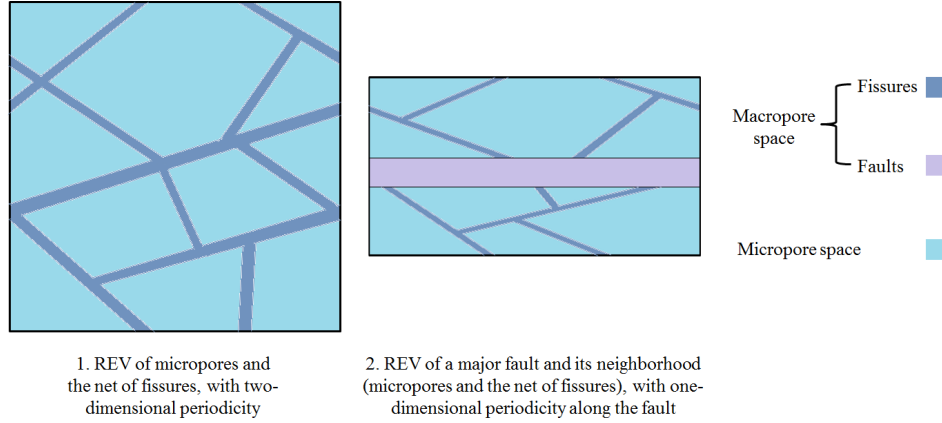
Fig. 1: Schematic representation of representative elementary volumes (REVs) of a fissured porous medium with pre-existing fault through double porosity model. REV 1 is a multi-dimensional periodic cell of standard double-porosity medium outside the major fault, with the net of fissures regarded as macropores and the voids in intact solid matrix as micropores. REV 2 is a cell of double-porosity medium of a fault neighborhood, with the major fault (induced by cracking, shear band formation, etc, and will be reactivated under mechanical forces or changes in pore pressure) regarded as macropore spaces in addition to the net of fissures. REV 2 has a one-dimensional periodicity along the fault. The formulation of multiscale finite element with embedded strong discontinuity in this paper makes use of the second REV.

Strong discontinuities such as grain boundaries, flaws, cracks, joints, and faults are very common across multiple length scales in geological materials. Understanding the hydro-mechanical responses of the interfaces is important for numerous engineering applications, such as oil exploration, geothermal applications, geological disposal of nuclear waste and CO2. The presence of strong discontinuities is important due to (1) their significant roles in altering the mechanical responses of the host system (e.g. strain localization, crack bands), (2) inducing anisotropic changes in the flow characteristics as they function as flow barrier (e.g. compaction band) or channels (e.g. tensile cracks), as well as (3) changing the hydro-mechanical coupling mechanisms under different loading conditions [Paterson and Wong, 2005, Sun et al., 2011a,b, Wibberley et al., 2016, Wang and Sun, 2017b].

A common approach to capture the hydro-mechanical responses is to use phenomenological laws designed for these interfaces [Xu and Needleman, 1994, Bishop, 2009, De Borst et al., 2012]. Within a finite element model, the interfaces are then either represented by surface elements inserted in between volume elements or enriched basis designed to captures the kinematics of the embedded strong discontinuities (e.g. assumed strain or extended finite element) within an element (e.g. Moës et al. [1999], Dolbow and Belytschko [1999], Callari and Armero [2002, 2004], Borja [2008], Liu and Borja [2008], Radovitzky et al. [2011], Sun et al. [2016], Rotunno et al. [2017]). Regardless of the techniques used to represent the strong discontinuities, the quality of the simulations strongly depends on the cohesive zone model chosen to represent the interfaces. However, as pointed out by Hirschberger et al. [2008] and exemplified in Park and Paulino [2011], many cohesive zone models are highly idealized constitutive responses where softening regimes are often curve-fitted via simple mathematical expressions (e.g. cubic polynomial, smoothed trapezoidal, exponential, and bilinear) to yield the right amount of fracture energy and stiffness. As a result, capturing the mixed-mode and cyclic responses remains a difficult task. Furthermore, the mixed-mode traction-separation is often an extension of the Mode I separation law where one simply uses an effective separation (defined as a function of normal and tangential displacement jumps) to determine the normal and tangen-

tial traction [Tvergaard and Hutchinson, 1992, Pandolfi et al., 2000]. In the case where effective separation is defined as a weighted norm of the normal and tangential component of the displacement jumps, the difference between Mode I crack and anti-crack cannot be captured. [Park and Paulino, 2011, Wang and Sun, 2017b]. This assessment has been also discussed in Belytschko et al. [2013] in which the complications due to the fact that unstable materials cannot maintain a homogeneous state even when the perturbation is small. This limitation is more profound when the interfaces possess multiscale microstructures where (1) meso-scale features such as voids and inclusions of sizes spanning multiple orders of magnitudes (e.g. the dual-porosity materials); (2) the microstructural length scale is comparable to the thickness of the interfaces (e.g. granular materials) and (3) when mixed-mode separation and closure happen cyclically.

The objective of this paper is to fill the alluded knowledge gaps via multiscale techniques designed specifically to capture the hydro-mechanical responses of interfaces in fluid-infiltrating porous materials in the finite deformation range. In particular, we introduce the computational homogenization procedure for dual-porosity porous layer based on the generalized effective stress principle. Extending the previous work in Liu et al. [2015], Wang and Sun [2016a,b], we establish micro-macro transitions to generate the proper hydro-mechanical responses from representative volume element (RVE) simulations as a replacement for the phenomenological traction-separation law and cubic laws for interfaces. Furthermore, as spatial averaging effective permeability of fractured porous system often leads to erroneous predictions on the flow characteristics, the interactions of the pore-fluid in the embedded strong discontinuities and that in the host porous matrix is captured via a dual-permeability system. As the porous media with strong discontinuities is viewed as a dual-permeability system at the macroscopic scale, a homogenization procedure is used to obtain the macro-pore, micro-pore and interfacial effective permeabilities [Le Garzic et al., 2011, Arbogast et al., 1990]. By considering the Hill-Mandel lemma for Darcy's flow in the macro- and micro-pore systems, admissible boundary conditions are defined such that both the macro- and micro-permeabilities can be estimated. Numerical examples are used to demonstrate the robustness and capacity of the multiscale poromechanics models. To the best knowledge of both authors, this is the first time a hierarchical discrete-continuum model has been established for embedded strong discontinuities in dual-permeability system undergoing large deformation.

The remainder of this paper is organized as follows. We first explain the kinematics of the dual-porosity, dual-permeability system with strong discontinuities. We then explain the various choices of RVE simulations with different boundary conditions that provide macroscopic hydro-mechanical responses for the interfaces. Following the description of the RVE simulations, we then describe the macroscopic finite element formulation with embedded discontinuity for dual-permeability systems. The implementation techniques are then highlighted, and numerical examples are presented. As for notations and symbols, bold-faced letters denote tensors; the symbol '·' denotes a single contraction of adjacent indices of two tensors (e.g. $\boldsymbol{a} \cdot \boldsymbol{b} = a_i b_i$ or $\boldsymbol{c} \cdot \boldsymbol{d} = c_{ij} d_{jk}$); the symbol ':' denotes a double contraction of adjacent indices of tensor of rank two or higher (e.g. $\boldsymbol{C} : \boldsymbol{\epsilon}^e = C_{ijkl} \epsilon_{kl}^e$); the symbol '⊗' denotes a juxtaposition of two vectors (e.g. $\boldsymbol{a} \otimes \boldsymbol{b} = a_i b_j$) or two symmetric second order tensors (e.g. $(\boldsymbol{\alpha} \otimes \boldsymbol{\beta})_{ijkl} = \alpha_{ij} \beta_{kl}$). Moreover, $(\boldsymbol{\alpha} \oplus \boldsymbol{\beta})_{ijkl} = \alpha_{jl} \beta_{ik}$ and $(\boldsymbol{\alpha} \ominus \boldsymbol{\beta})_{ijkl} = \alpha_{il} \beta_{jk}$. We also define identity tensors $(\boldsymbol{I})_{ij} = \delta_{ij}$, $(\boldsymbol{I}^4)_{ijkl} = \delta_{ik} \delta_{jl}$, and $(\boldsymbol{I}_{\text{sym}}^4)_{ijkl} = \frac{1}{2}(\delta_{ik} \delta_{jl} + \delta_{il} \delta_{kj})$, where δ_{ij} is the Kronecker delta. As for sign conventions, unless specify otherwise, we consider the direction of the tensile stress and dilative pressure as positive.

2 Problem Statement

This section provides a brief account of the theoretical basis of the multi-scale coupling model designed for a dual-porosity, dual-permeability system with embedded strong discontinuities. While there are previous work dedicated to model embedded strong discontinuities of porous media in the small and finite deformation ranges (e.g. Steinmann [1999], Larsson and Larsson [2000], Callari and Armero [2004], Mosler [2006], Mohammadnejad and Khoei [2013], Sun et al. [2016], Nikolic et al. [2016], de Borst [2016], Prevost and Sukumar [2016], de Borst [2017a]), there has not yet been any attempt to introduce bridging-scale methods for interfaces composed of dual-porosity, dual-permeability materials. Nor is there any work aimed at introducing constitutive responses via discrete-continuum coupling to simultaneously replace phenomenological cohesive zone law and anisotropic permeability model for interfaces in the finite deformation range. In this section, we first briefly review the kinematics of the hydro-mechanical interfaces.

Following this, a brief description of the boundary value problem for the dual-permeability system in finite deformation range and that of the corresponding finite element formulation of interfaces are given.

2.1 Large-scale dual-permeability hydro-mechanical problem

Consider a saturated porous medium with highly localized deformation zones (e.g. cracks, faults.) occupying a spatial domain $\mathcal{B} \subset \mathbb{R}^{n_{sd}}$, where $n_{sd} = 1, 2,$ or 3 stands for the number of spatial dimensions. The boundary of the body in the reference configuration is denoted as $\partial \mathcal{B} \subset \mathbb{R}^{n_{sd}-1}$. The porous solid is treated as a double-porosity mixture and the two dominant pore scales are the macropores M (in this case the pores of fissures, shear bands, cracks) and the micropores m, (micro-pores in the solid matrix). A solid skeleton material point at point X of the reference configuration may move due to rigid body motion and/or deformation. Here we assume that this material point is defined in a macroscopic sense such that the material point is associated with a representative elementary volume whose space is partially occupied by the solid constituent and the fluid constituent in the macro- and micro-pores. For convenience, the microstructural attributes of this representative elementary volume are often neglected and the porous medium is therefore regarded as a multiphase effective medium. If no crack growth or healing occurs, the location of this material point in the current configuration can be determined via the mapping $x = \boldsymbol{\varphi}(X, t)$. The displacement is $\boldsymbol{u}(X, t) = \boldsymbol{x}(X, t) - X = \boldsymbol{\varphi}(X, t) - X$. The macroscopic deformation of the effective medium is therefore characterized by $\boldsymbol{F} = \frac{\partial \boldsymbol{\varphi}}{\partial X} = \nabla^X \boldsymbol{\varphi}$. The elementary volumes of the total mixture, solid, macropores, micropores and void are denoted as dV, dV_s, dV_M, dV_m, $dV_v = dV - dV_s = dV_M + dV_m$, respectively. The pore fractions for macropores (ψ^M) and micropores (ψ^m) are defined as,

$$\psi^M(X, t) = \psi = \frac{dV_M}{dV_v}, \quad \psi^m(X, t) = 1 - \psi = \frac{dV_m}{dV_v}. \tag{1}$$

Meanwhile, the volume fractions for solid, macropores and micropores can be expressed as a function of porosity and pore fractions, i.e.,

$$\begin{aligned}
\phi(X, t) &= \frac{dV_v}{dV}, \\
\phi^s(X, t) &= \frac{dV_s}{dV} = 1 - \phi, \\
\phi^M(X, t) &= \frac{dV_M}{dV} = \phi\psi, \\
\phi^m(X, t) &= \frac{dV_m}{dV} = \phi(1 - \psi).
\end{aligned} \tag{2}$$

The partial mass densities of each constituent can be determined using the volume fractions and the intrinsic mass density of solid ρ_s and fluid ρ_f:

$$\begin{aligned}
\rho^s &= \phi^s \rho_s = (1 - \phi)\rho_s, \\
\rho^M &= \phi^M \rho_f = \phi\psi\rho_f, \\
\rho^m &= \phi^m \rho_f = \phi(1 - \psi)\rho_f.
\end{aligned} \tag{3}$$

The pull-back total mass density of the mixture is given by

$$\rho_0 = \rho_0^s + \rho_0^M + \rho_0^m = J\rho^s + J\rho^M + J\rho^m, \tag{4}$$

where $J = \det(\boldsymbol{F})$ is the Jacobian of the solid motion.

Let us denote the (solid) material time derivative following the solid skeleton trajectory as $(\dot{\bullet}) = \frac{\partial(\bullet)}{\partial t} + \nabla^x(\bullet) \cdot \boldsymbol{v}$. Assuming incompressible solid and fluid constituents and no mass exchange between solid and fluid [Borja and Choo, 2016]:

$$\begin{aligned}
\dot{\rho}_0^M &= \overline{J\phi\dot{\psi}\rho_f} = \dot{J}\psi\rho_f + J\phi\dot{\psi}\rho_f = \rho_f J\psi \nabla^x \cdot \boldsymbol{v} + \rho_f J\phi\dot{\psi}, \\
\dot{\rho}_0^m &= \overline{J\phi(1 - \psi)\rho_f} = \dot{J}(1 - \psi)\rho_f - J\phi\dot{\psi}\rho_f = \rho_f J(1 - \psi) \nabla^x \cdot \boldsymbol{v} - \rho_f J\phi\dot{\psi},
\end{aligned} \tag{5}$$

144 using the identities $\overline{\dot{J}\phi} = \dot{J} - \overline{\dot{J}\phi^s} = \dot{J}$ and $\dot{J} = J\nabla^x \cdot v$ [Song and Borja, 2014].

145 The relative fluid mass fluxes q_M, q_m, and relative fluid velocities $\widetilde{v}_M$, $\widetilde{v}_m$ take the form

$$
\begin{aligned}
q_M &= \rho^M \widetilde{v}_M &&= \rho_f \phi \psi \, \widetilde{v}_M &&= \rho_f \phi \psi \, (v_M - v), \\
q_m &= \rho^m \widetilde{v}_m &&= \rho_f \phi (1 - \psi) \, \widetilde{v}_m &&= \rho_f \phi (1 - \psi) \, (v_m - v),
\end{aligned}
\tag{6}
$$

146 where v_M and v_m are the fluid velocities in the macropores and micropores, respectively.

147 The relative fluid mass fluxes are related to pore pressures via Darcy's law:

$$
\begin{aligned}
q_M &= -\rho_f \frac{k_M}{\mu_f} \cdot (\nabla^x p_M - \rho_f g), \\
q_m &= -\rho_f \frac{k_m}{\mu_f} \cdot (\nabla^x p_m - \rho_f g),
\end{aligned}
\tag{7}
$$

148 where p_M and p_m are Cauchy macropore pressure and Cauchy micropore pressure, respectively. k_M and
149 k_m are intrinsic permeability tensors for macro-scale pore and micro-scale pore. μ_f is the dynamic viscosity
150 of the fluid. g is the gravity acceleration vector.

151 The pull-back mass fluxes are obtained by Piola transforms

$$
Q_M = JF^{-1} \cdot q_M, \quad Q_m = JF^{-1} \cdot q_m.
\tag{8}
$$

152 The fluid in macropores can diffuse from or into micropores. The fluid mass transfer between the two
153 scales is characterized by the coefficient [Choo et al., 2016]

$$
c_0 = Jc = J\frac{\bar{\alpha}}{\mu_f}(p_M - p_m).
\tag{9}
$$

154 $\bar{\alpha}$ is a material parameter for macro-micro-pore interface permeability.

155 To construct the strong form of the problem, the boundary $\partial\mathcal{B}$ having unit normal N at $X \in \partial\mathcal{B}$ admits
156 the decomposition

$$
\begin{cases}
\partial\mathcal{B} = \overline{\partial\mathcal{B}_u \cup \partial\mathcal{B}_t} = \overline{\partial\mathcal{B}_{p_M} \cup \partial\mathcal{B}_{q_M}} = \overline{\partial\mathcal{B}_{p_m} \cup \partial\mathcal{B}_{q_m}} \\
\varnothing = \partial\mathcal{B}_u \cap \partial\mathcal{B}_t = \partial\mathcal{B}_{p_M} \cap \partial\mathcal{B}_{q_m} = \partial\mathcal{B}_{p_M} \cap \partial\mathcal{B}_{q_m}
\end{cases},
\tag{10}
$$

157 where $\partial\mathcal{B}_u$, $\partial\mathcal{B}_{p_M}$ and $\partial\mathcal{B}_{p_m}$ are Dirichlet boundaries with prescribed solid displacement, macropore pres-
158 sure and micropore pressure, respectively. $\partial\mathcal{B}_t$, $\partial\mathcal{B}_{q_M}$ and $\partial\mathcal{B}_{q_m}$ are Neumann boundaries with prescribed
159 tractions, macropore flux and micropore flux, respectively.

160 Assuming quasi-static case and incompressible solid and fluid constituent, the Lagrangian strong form
161 of the large-scale dual-permeability hydro-mechanical problem reads: find the displacement $u : \mathcal{B} \to \mathbb{R}^{n_{sd}}$,
162 the Cauchy macropore pressure $p_M : \mathcal{B} \to \mathbb{R}$ and the Cauchy micropore pressure $p_m : \mathcal{B} \to \mathbb{R}$ such that the
163 balance of linear momentum, the balance of mass in macropores and micropores, the boundary conditions
164 are satisfied:

$$
\begin{cases}
\nabla^X \cdot P + \rho_0 g = c_0(\widetilde{v}_m - \widetilde{v}_M) & \text{on } \mathcal{B}, \\
\dot{\rho}_0^M + \nabla^X \cdot Q_M = -c_0 & \text{on } \mathcal{B}, \\
\dot{\rho}_0^m + \nabla^X \cdot Q_m = c_0 & \text{on } \mathcal{B}, \\
u = \hat{u} & \text{on } \partial\mathcal{B}_u \\
P \cdot N = \hat{t} & \text{on } \partial\mathcal{B}_t, \\
p_M = \hat{p}_M & \text{on } \partial\mathcal{B}_{p_M}, \\
Q_M \cdot N = -\hat{Q}_M & \text{on } \partial\mathcal{B}_{q_M}, \\
p_m = \hat{p}_m & \text{on } \partial\mathcal{B}_{p_m}, \\
Q_m \cdot N = -\hat{Q}_m & \text{on } \partial\mathcal{B}_{q_m},
\end{cases}
\tag{11}
$$

where P is the first Piola-Kirchhoff stress and its relation to Kirchhoff stress tensor τ and Cauchy stress σ are:

$$\tau = J\sigma = P \cdot F^{\mathrm{T}}. \tag{12}$$

The total Kirchhoff stress tensor permits the following decomposition in terms of effective Kirchhoff stress τ' and Cauchy pore pressures p_M and p_m, based on the effective stress principle,

$$\tau = \tau' - Jp^{\mathrm{avg}}I = \tau' - J[\psi p_M + (1 - \psi)p_m]I. \tag{13}$$

The initial conditions are imposed as

$$u(X) = u_0(X), \ p_M(X) = p_{M_0}(X), \ p_m(X) = p_{m_0}(X) \text{ for all } X \in \mathcal{B} \text{ at } t = t_0. \tag{14}$$

2.2 Kinematics of embedded strong discontinuities in dual-permeability porous media

Consider a material point X in the dual-permeability porous media $\mathcal{B}$ and an associated local neighborhood $\mathcal{B}_X \subset \mathcal{B}$ embedded with strong discontinuity (fracture, shear band, fault, etc.). Denote the surface of discontinuity as Γ and the local domain $\mathcal{B}_X$ is thus divided by Γ into sub-domain pair $\mathcal{B}_X = \mathcal{B}_X^+ \bigcup \mathcal{B}_X^-$. The motion of the particles within $\mathcal{B}_X$ is described by local displacement field $u_\Gamma = x_\Gamma - X = \varphi_\Gamma(X) - X$. Assume the following relation to the large-scale (or conformal) displacement field u,

$$u_\Gamma = u + [\![u]\!](H_\Gamma - f_\Gamma), \tag{15}$$

where $[\![u]\!]$ is the displacement jump across the interface Γ, H_Γ is the Heaviside step function across Γ and f_Γ is a smooth ramp function in $\mathcal{B}_X$ [Borja, 2002]. It is also useful to define the continuous part $\bar{u}$ of motion u_Γ as

$$\bar{u} = u - [\![u]\!] f_\Gamma. \tag{16}$$

The large-scale (or conformal) and continuous deformation gradients are defined as,

$$F = I + \nabla^X u, \quad \overline{F} = I + \nabla^X \bar{u}. \tag{17}$$

The local deformation gradient is given by, assuming relative uniformity of $[\![u]\!]$ along Γ such that $\nabla^X [\![u]\!] \rightarrow 0$ in $\mathcal{B}_X$,

$$\begin{aligned}
F_\Gamma &= I + \nabla^X u_\Gamma \\
&= F - [\![u]\!] \otimes \nabla^X f_\Gamma + ([\![u]\!] \otimes N)\delta_\Gamma \\
&= \overline{F} + ([\![u]\!] \otimes N)\delta_\Gamma,
\end{aligned} \tag{18}$$

where the equation $\nabla^X H_\Gamma = \delta_\Gamma N$ is employed. δ_Γ is the Dirac delta function across Γ and N is the unit normal of Γ pointing from $\mathcal{B}_X^-$ to $\mathcal{B}_X^+$.

From Eq. 18, following Armero and Garikipati [1996], Callari and Armero [2004], Armero and Linder [2008], the local deformation gradient allows a multiplicative decomposition into two parts:

$$F_\Gamma = \overline{F} \cdot \widetilde{F} = \overline{F} \cdot (I + ([\![U]\!] \otimes N)\delta_\Gamma) \tag{19}$$

where $[\![U]\!] = \overline{F}^{-1} \cdot [\![u]\!]$ is the material displacement jump across Γ.

The presence of displacement jump in the solid phase results in the discontinuity of the fluid flux across the interface. The localized fluid flow model developed by [Callari and Armero, 2002, 2004] states that the fluid flux vector field Q_Γ in the local neighborhood $\mathcal{B}_X$ is composed of a regular flow field Q and a local flux jump $[\![Q]\!]$:

$$Q_\Gamma = Q + [\![Q]\!](H_\Gamma - f_\Gamma). \tag{20}$$

The same ramp function f_Γ as in the displacement field is employed, but a different ramp function can also be chosen. The rate of local fluid content M_Γ (fluid mass increment per unit reference volume of porous solid) is thus obtained by

$$\dot{M}_\Gamma = -\nabla^X \cdot Q_\Gamma = -\nabla^X \cdot Q + [\![Q]\!] \cdot \nabla^X f_\Gamma - ([\![Q]\!] \cdot N)\delta_\Gamma, \tag{21}$$

194 with the assumption of $\nabla^X \cdot [\![Q]\!] \to 0$ in $\mathcal{B}_X$. In this model, the mass flux could be discontinuous across
195 the interface, while the pressure field remains continuous. This assumption is justified by the experimental
196 findings that in ordinary soil mechanics testing situations or for quasi-static loading conditions, no pore-
197 water pressure shocks can develop across shear band boundaries [Vardoulakis, 1996]. The assumption
198 is also a necessary condition for the existence of second order derivative of pore pressures as shown in
199 Equations (7), (21). This assumption allows for storage and fluid flow within the discontinuity, but the
200 interface permeability must be infinitely large. Moreover, since there is no independent pressure inside the
201 interface, the model also lacks the capability to simulate the pressurized crack [de Borst, 2017b].

202 To circumvent this issue described in de Borst [2017b], we introduce a simplified effective-medium
203 approach in which pores inside the major fault (strong discontinuity), the nearby net of fissures and the
204 intact host continuum are idealized as two porous systems of distinct pore sizes. The pore spaces inside
205 the strong discontinuities and fissures constitute the macropore system, whereas the pore spaces inside
206 the intact continuum are considered as the micropore system. Those porous systems may exchange fluid
207 mass. Assuming that the separation of scales applies and there exists an appropriate length scale such
208 that the fissured porous media can be treated as the superimposition of three continua, the solid skeleton,
209 the macro-fluid continuum and the micro-fluid continuum at the representative elementary volume level.
210 Then the pore pressure and fluid flux of each pore system could be distinctive until both porous systems
211 reach steady state. In this treatment, the detailed fluctuation of the micro- and macro-pore fluid flow be-
212 low the scale of the RVE is ignored. Nevertheless, this treatment also enables us to capture the transient
213 fluid responses across distinct time and spatial scales. This capacity is particularly important to deal with
214 dual-permeability media with significant permeability differences and/or when the mass exchange is slow
215 compared to the flux in either porous system (e.g. the pressurized crack).

216 Assuming that the homogenization procedure is valid even if an embedded strong discontinuity exists,
217 then the pore pressure and flux fields can be defined at the macroscopic continuum scale such that p_M
218 and Q_M are the macroscopic macropore pressure and flux of the effective porous system that represents
219 all the macropore space inside the net of fissures and the major fault. Meanwhile, p_m and Q_m are the
220 pressure and flux of the effective porous system that represents the micropore space inside the intact solid
221 skeleton. Furthermore, the transfer flow at the continuum scale can be idealized as the flow between the
222 effective porous system that represents the pore space inside intact solid skeleton and the counterpart that
223 simultaneously represents both the pore space of the fault and the fissures.

224 p_M, p_m and Q_M, Q_m are continuous fields obtained from separate balance equations of fluid mass in
225 both pore-scales, interconnected by the fluid mass transfer c_0 between the two pores (Eq. 11). For finite
226 elements with embedded strong discontinuity, standard integrations are employed for all pressure and
227 fluid flow in macropores and micropores. Note that this treatment employed in the proposed framework
228 is not the only feasible approach. In the case where sub-scale fluctuations of pore pressure and flux are
229 important, one may consider the localized fluid flux formulation previously established in Callari and
230 Armero [2004].

231 2.3 Condition of traction continuity

232 The solution of the local displacement jump field $[\![u]\!]$ requires a traction continuity equation relating the
233 nominal stress field P in $\mathcal{B}_X \setminus \Gamma$ and the nominal traction T_Γ in Γ driving the mechanical inelastic effects
234 inside the strong discontinuity. The weak form writes, for all variations $\delta [\![u]\!]$, [Armero, 1999]

$$-\frac{1}{V_{\mathcal{B}_X}} \int_{\mathcal{B}_X} \delta [\![u]\!] \cdot PN \, dV + \frac{1}{L_\Gamma} \int_\Gamma \delta [\![u]\!] \cdot T_\Gamma \, d\Gamma = 0, \tag{22}$$

235 where $V_{\mathcal{B}_X} = \text{measure}(\mathcal{B}_X)$ and $L_\Gamma = \text{measure}(\Gamma)$. Since the fluid pressure in both pore-scales are contin-
236 uous across the strong discontinuity, $[\![p_M]\!] = 0$, $[\![p_m]\!] = 0$, Eq. 22 can be written in terms of effective stress
237 and traction:

$$-\frac{1}{V_{\mathcal{B}_X}} \int_{\mathcal{B}_X} \delta [\![u]\!] \cdot P'N \, dV + \frac{1}{L_\Gamma} \int_\Gamma \delta [\![u]\!] \cdot T'_\Gamma \, d\Gamma = 0. \tag{23}$$

In the limit $\frac{V_{B_X}}{L_\Gamma} \to 0$, the local equilibrium equation writes:

$$T'_\Gamma = (P' \cdot N)|_\Gamma. \tag{24}$$

The effective stress measure P' in the host continuum just outside the strong discontinuity is determined by the continuous part of the total deformation gradient, i.e., $P' = P'(\overline{F}) = P'(F, [\![u]\!])$. The effective traction measure is given by the displacement jump, i.e., $T'_\Gamma = T'_\Gamma([\![u]\!])$. These two constitutive laws for the host continuum and for the fracture are presented in the subsequent section.

2.4 Constitutive equations

Inelastic dissipation mainly occurs inside the strong discontinuities of a solid body under external loading, while the host matrix outside these localized zones remains intact. Thus, to reduce computational cost, the multi-scale approach is only adopted in the vicinity of strong discontinuities, and we assume a Neo-Hookean hyperelastic constitutive model is sufficient to replicate the constitutive responses of the host matrix. For a RVE associated with a material point undergoing a deformation characterized by the Left Cauchy-Green deformation tensor $b = F \cdot F^T = \overline{F} \cdot \overline{F}^T$, the effective Kirchhoff stress is given by [Belytschko et al., 2013],

$$\tau' = \lambda_0 \ln J \, I + \mu_0(b - I), \tag{25}$$

where λ_0 and μ_0 are the Lamé constants from linear elasticity.

The spatial elasticity tensor $\mathcal{C}^e$ is given by

$$\mathcal{C}^e = \lambda_0 I \otimes I + 2(\mu_0 - \lambda_0 \ln J)I^4_{\text{sym}}. \tag{26}$$

$\mathcal{C}^e$ relates the Lie derivative of the effective stress tensor to the velocity gradient, i.e., $\mathscr{L}_v \tau' = \mathcal{C}^e : d = \mathcal{C}^e : \frac{1}{2}(\nabla^x v + v \nabla^x) = \mathcal{C}^e : \nabla^x v$, after noting the minor symmetry of $\mathcal{C}^e$. Then the spatial tensor α^e with respect to the rate of τ' is given by

$$\dot{\tau}' = \alpha^e : \nabla^x v, \quad \alpha^e = \mathcal{C}^e + \tau' \oplus I + \tau' \ominus I. \tag{27}$$

The material parameters for the model can be determined by numerical experiments on an initial micro-scale representative volume element (RVE) composed of discrete particles: a uniaxial tension/compression test to get the P-wave modulus M and a simple shear test to get the shear modulus G. Then $\lambda_0 = M - 2G$ and $\mu_0 = G$.

As for the traction-separation relation $T'_\Gamma = T'_\Gamma([\![u]\!])$ for the strong discontinuity, it is homogenized from the micro-scale RVE, and the approach is detailed in the subsequent section.

The material properties for the dual-porosity hydraulic model are obtained as follows. The permeability tensor k_M in macropores (fractures) in Eq. (7) is given by machine learning model trained with permeability data from Lattice-Boltzmann simulation on micro-scale RVE, as explained in Section 3. Since the microscale RVE only represents the medium inside the strong discontinuity, the hydraulic properties for the host medium and mass transfer between the two media remain updated from phenomenological laws. The permeability tensor k_m in micropores (host matrix) is assumed isotropic and its evolution against the micro-porosity follows the Kozeny–Carman relation,

$$k_m = k_m I, \; k_m = k_{m0} \frac{\phi_m^3/(1 - \phi_m)^2}{\phi_{m0}^3/(1 - \phi_{m0})^2}, \tag{28}$$

where k_{m0} is the initial permeability for the solid matrix having initial micro-porosity of ϕ_{m0}. The pore fraction ψ for macropores (the ratio between the pore volumes of fissures and the total porous continuum) is assumed to be constant during the deformation of the continuum. Thus the current value of macroporosity is obtained as, assuming incompressible solid phase, $\phi^M = \psi\phi = \psi[1 - (1 - \phi_0)J^{-1}]$, and $\phi^m = (1 - \psi)\phi = (1 - \psi)[1 - (1 - \phi_0)J^{-1}]$.

The mass transfer coefficient $\bar{\alpha}$ in Eq. (9) is a dimensionless parameter that depends on the permeability of the interface between macropores and micropores $\bar{k}$, as well as characteristic length of the macropores

spacing and solid matrix geometry [Callari and Federico, 2000, Choo and Borja, 2015, Borja and Choo, 2016]. The interface permeability $\bar{k}$ is assumed to equal to the micropore permeability k_m, following the same assumption as Lewandowska et al. [2004], Choo and Borja [2015]. If the effect of the geometry of the strong discontinuity is considered in the mass transfer term, $\bar{\alpha}$ should become a tensor $\bar{\boldsymbol{\alpha}}$ instead of a scalar to take into account the preferential mass transfer direction normal to the interface, in addition to the assumed isotropic mass transfer between the net of fissure and the micropore space. Hence Equation (9) is modified to a tensor form,

$$c_0 = Jc = \frac{J}{3\mu_f}\bar{\boldsymbol{\alpha}} : (p_M \boldsymbol{I} - p_m \boldsymbol{I}). \tag{29}$$

where $\bar{\boldsymbol{\alpha}}$ is now a homogenized mass transfer coefficient tensor including the structural information of the interfaces between macropores and micropores. A simple form of $\bar{\boldsymbol{\alpha}}$ can be defined as

$$\bar{\boldsymbol{\alpha}} = \frac{dV_{fissure}}{dV_M}\bar{\alpha}\boldsymbol{I} + \frac{dV_{SD}}{dV_M}\bar{\alpha}\boldsymbol{n} \otimes \boldsymbol{n}, \tag{30}$$

where $dV_{fissure}$ and dV_{SD} are elementary volumes of the net of fissures and the strong discontinuity in the macropore space dV_M, respectively.

3 Computational homogenization for strong discontinuity

Here we present the procedure to obtain the hydro-mechanical constitutive updates for embedded strong discontinuity from microscale simulations on RVEs nested inside the material interfaces. The computational homogenization schemes of single-physics material layers have been explored in a number of previous studies [Hirschberger et al., 2009, Coenen et al., 2012, Bosco et al., 2014, Wang and Sun, 2018]. For instance, Hirschberger et al. [2009] have introduced a procedure to generate an effective cohesive zone law for a single interface from microscale RVE. In those studies, FE^2 simulations with interface elements are used as the test bed. Coenen et al. [2012], Bosco et al. [2014] establish a multi-scale approach for RVE (or Microstructural Volume Element as introduced in the literature) having localized zones and proposed a new generalized periodic boundary condition. The overall macro-homogeneous deformation is applied to the MVE and the stress and displacement jump are homogenized. The local equation to be solved is the consistency between the macro displacement jump and the homogenized displacement jump in the RVE, instead of the traction continuity equation. Toro et al. [2014, 2016] proposed multiscale model at regular points (MMRp) and singular points (MMSp). It has been successfully used in enhanced strain finite element simulations [Oliver et al., 2015]. In this study, the RVEs of discrete elements describe the underlying microstructures inside the discontinuity interface. Based on the effective stress principle, the mechanical and hydraulic constitutive laws are obtained **separately** from two types microscale simulations, i.e. the grain-scale DEM simulation and the pore-scale LBM simulation, as explained in Sun et al. [2013] and Wang and Sun [2016a]. In other words, the effective traction and the interfacial permeability (and hence the interfacial Darcy's velocity) are both obtained from the same deformed configuration. However, the deformed configuration is not obtained from LBM-DEM simulations but from DEM simulations that generate the admissible boundary conditions by assuming the validity of the effective stress principle. The major advantage of this approach is two-fold. First, the calculations of the interfacial permeability are much faster. This is due to the fact that the de-coupled permeability calculation can be conducted offline such that the trained and validated neural network can be used to replace the costly LB simulations). The second advantage is the simplicity. As the effective stress approach does not require the introduction of particle-scale hydro-mechanical force and any treatment to update the fluid-solid boundary at pore scale. Nevertheless, it should be noted that the validity of this split approach is designed for the case in which the effective stress principle is applicable for the dual-permeability system. In many situations that involve particle erosion [Galindo-Torres et al., 2015, Tran et al., 2017], soil liquefaction [El Shamy and Abdelhamid, 2014], or solid-fluid mixture with non-Darcy flow or high Reynold's number, such a simplification may lead to significant errors. In such cases, one must derive the corresponding Hill-Mandel condition for the multi-physical poromechanics problems to obtain the admissible boundary conditions and apply them to the DEM-LBM model or use direct numerical simulation (DNS) to capture the multi-physical problems. Such an extension will be considered in the future study but is out of the scope of this work.

The Hill-Mandel condition and the corresponding computational homogenization procedure that calculates the homogenized effective traction and interfacial permeability measures in the finite deformation enhanced strain formulation are detailed in the following sub-sections.

3.1 Online incremental homogenized mechanical responses for strong discontinuities

The homogenization procedure of mechanical constitutive law is an extension of the approach described in [Hirschberger et al., 2009] to particle assembly using the theory in [Miehe and Dettmar, 2004, Miehe et al., 2010]. Consider a cubic assembly of discrete particles representing the granular material inside the strong discontinuity (Fig. 2). The body force is negligible at micro-scale. This RVE of domain Ω_μ and boundary $\partial\Omega_\mu$ has an initial height of h_μ^0 and is associated with a coordinate system with basis vectors M_μ and N_μ. Choose the geometric center as the origin and place the RVE in alignment with the normal and tangential directions of the strong discontinuity Γ in the reference configuration ($N_\mu = N$, $M_\mu = M$). The current position x_μ^c of a center of a particle is related to its position X_μ^c in the reference configuration via the deformation map $\boldsymbol{\varphi}_\mu$. The local deformation gradient $F_\mu = \frac{\delta \boldsymbol{\varphi}_\mu}{\delta X_\mu^c}$. The volume average of F_μ is given as:

$$\langle F_\mu \rangle = \frac{1}{V_0} \int_{\Omega_\mu} F_\mu \, d\Omega_\mu = \frac{1}{V_0} \sum_i^{N_{bound}} (x_\mu^c)_i \otimes A_i^c, \tag{31}$$

where V_0 is the initial volume of the RVE. A_i^c is the surface vector of $\partial\Omega_\mu$ associated with the particle i and N_{bound} is the number of particles on $\partial\Omega_\mu$. Assuming rigid particles, the motion of a particle material point can be decomposed to the motion of the particle center and the particle rotation, i.e.,

$$x_\mu = x_\mu^c + R_\mu \cdot (X_\mu - X_\mu^c); \quad x_\mu^c = \langle F_\mu \rangle \cdot X_\mu^c + w_c, \tag{32}$$

where w_c is the particle center displacement fluctuation and $R_\mu \in SO(3)$ describes the particle rotation.

The overall effective Piola stress is given by the volume average

$$\langle P_\mu' \rangle = \frac{1}{V_0} \int_{\Omega_\mu} P_\mu' \, d\Omega_\mu = \frac{1}{V_0} \sum_{cont}^{N_{cont}} f_\mu^{cont} \otimes L_\mu^{cont} = \frac{1}{V_0} \sum_i^{N_{bound}} (f_\mu^{ext})_i \otimes (X_\mu^c)_i, \tag{33}$$

where f_μ^{cont} is the contact force at the grain contact x_μ^{cont}. L_μ^{cont} is the initial branch vector, the vector that connects the centroids of two grains forming the contact. N_{cont} is the total number of particles contacts in the RVE. $(f_\mu^{ext})_i$ is the external support force acting on the boundary particle i. The transition between the summation involving contact forces and the summation involving external support forces is ensured by the equilibrium of the RVE of particles.

The volume average of the virtual power in the RVE is given by

$$\langle P_\mu' : \dot{F}_\mu \rangle = \frac{1}{V_0} \int_{\Omega_\mu} P_\mu' : \dot{F}_\mu \, d\Omega_\mu = \frac{1}{V_0} \sum_i^{N_{bound}} (f_\mu^{ext})_i \cdot (\dot{x}_\mu^c)_i. \tag{34}$$

The Hill-Mandel micro-heterogeneity condition requires the volume average of the virtual power in the RVE to equal the virtual power done by the volume averages of power-conjugate stress and deformation measures:

$$\langle P_\mu' : \dot{F}_\mu \rangle = \langle P_\mu' \rangle : \langle \dot{F}_\mu \rangle. \tag{35}$$

Since the constitutive behavior of the RVE is homogenized to a traction-separation law on the interface, the Hill-Mandel condition is recast into the form involving power-conjugate effective traction and displacement jump measures

$$h_0 \langle P_\mu' : \dot{F}_\mu \rangle = \langle T_\Gamma' \rangle \cdot \mathscr{L}_v [\![u]\!] = \langle \mathscr{T}_\Gamma \rangle \cdot [\![\dot{U}]\!]. \tag{36}$$

For the transition between the macro-scale kinematics of the strong discontinuity and the deformation of the micro-scale RVE, the volume average of deformation gradient is defined as

$$\langle \boldsymbol{F}_\mu \rangle = \boldsymbol{I} + \frac{1}{h_\mu^0} [\![\boldsymbol{u}]\!] \otimes \boldsymbol{N}. \tag{37}$$

The effective nominal traction $\langle \boldsymbol{T}_\Gamma' \rangle$ averaged in the RVE representing the interface is given by:

$$\langle \boldsymbol{T}_\Gamma' \rangle = \langle \boldsymbol{P}_\mu' \rangle \cdot \boldsymbol{N}. \tag{38}$$

Among the admissible boundary conditions fulfilling the Hill-Mandel micro-heterogeneity condition, we adopt the periodic boundary conditions, where for a pair of particles on opposite boundaries $\partial \mathcal{V}^+$ and $\partial \mathcal{V}^-$, the periodicity enforces the periodicity of fluctuations and rotations

$$\boldsymbol{w}_c^- = \boldsymbol{w}_c^+, \quad \boldsymbol{R}_\mu^- = \boldsymbol{R}_\mu^+, \tag{39}$$

and the anti-periodicity of support forces and couples

$$\boldsymbol{a}_c^- = -\boldsymbol{a}_c^+, \quad \boldsymbol{m}_c^- = -\boldsymbol{m}_c^+, \tag{40}$$

where $\boldsymbol{a}_c$ is the opposite of the resultant force on the boundary particle exerted by other particles, $\boldsymbol{m}_c$ is the opposite of the resultant couple about the center $\boldsymbol{X}_c$ on the boundary particle.

3.2 Offline incremental data-driven hydraulic responses for strong discontinuities

The homogenization procedure used to obtain the effective permeability from a microstructure RVE has been previously studied in Du and Ostoja-Starzewski [2006], Ostoja-Starzewski et al. [2007], Sun et al. [2011a, 2013]. Here we apply the same procedure to obtain the homogenized effective permeability of the embedded strong discontinuities. Assume that the separation of the spatial length scale is valid, one may use the Hill-Mandel lemma corresponding to Darcy's flow problem to determine the admissible boundary condition for the flow problems. Recall that the Hill-Mandel lemma requires that

$$\langle \nabla^x p_M \cdot \boldsymbol{q}_M \rangle_x = \langle \nabla^x p_M \rangle_x \cdot \langle \boldsymbol{q}_M \rangle_x \tag{41}$$

where $\langle \cdot \rangle_x$ is the spatial volume averaged operator.

As shown in Du and Ostoja-Starzewski [2006] and Ostoja-Starzewski et al. [2007], this can lead to a number of admissible boundary conditions. For instance, one may either prescribe flux or pore pressure gradient in two opposite faces of the RVEs. One interesting aspect found in previous works (cf. Du and Ostoja-Starzewski [2006], Sun et al. [2011a, 2013], Kuhn et al. [2015]) is that the choice of the boundary condition does not affect the effective permeability once the size of the RVE is sufficiently large. As mentioned previously in Section 2.2, we follow the treatment in de Borst [2017b] and assume that there is no pore pressure jump across the interface, whereas discontinuous mass flux is admissible.

The effective permeability tensor of a RVE can be determined via inverse fluid flow problem performed on the deformed RVE subjected to prescribed loading paths. The Eulerian fluid flux vector $\boldsymbol{q}$ within the RVE is computed when subjected to Eulerian pressure gradient $\nabla^x p$, and the macro-pore effective permeability $\boldsymbol{k}_{\mathrm{RVE}}^M$ is determined by Darcy's law

$$\boldsymbol{q}_M = -\frac{1}{\mu} \boldsymbol{k}_{\mathrm{RVE}}^M \nabla^x p_M. \tag{42}$$

μ is the dynamic viscosity of the fluid. We assume that the normal and tangential directions of the interface are also the principal directions of the macro-pore effective permeability tensors. Thus, we need only two hydraulic simulations to determine the permeability values normal and tangential to the interface, denoted as k_n^M and k_m^M, respectively. Thus the permeability tensor is expressed as

$$\boldsymbol{k}_{\mathrm{RVE}}^M = k_n^M \boldsymbol{n} \otimes \boldsymbol{n} + k_m^M \boldsymbol{m} \otimes \boldsymbol{m}, \tag{43}$$

where $n = \overline{F} \cdot N$ and $m = \overline{F}^{-T} \cdot M$. We choose the lattice Boltzmann (LB) method to solve the inverse fluid flow problem. For brevity, we omit the description of the LB method. Interested readers are referred to Sun et al. [2011b, 2013] and Kuhn et al. [2015] for details. The LB code used in this study is a C++ open source code called Palabos [Degruyter et al., 2010]. The procedure to obtain the two normal and tangential components is as follows. We first record the positions of all grains in the deformed microstructural assembly at different strain levels. As the size of each grain is known, the configuration of the pore space can be reconstructed and subsequently converted into binary images (cf. Sun et al. [2013]). Then, pore pressure difference is imposed on two opposite sides orthogonal to the flow direction and no-flow boundary conditions are applied on the four remaining side faces. This setting leads to a macroscopic pressure gradient. As the lattice Boltzmann flow simulation reaches steady state, the resultant fluid flow velocity is computed and the permeability value is derived via Darcy's law (Fig. 2). Fig. 5 illustrates an example computation of permeabilities from LBM. The RVE is subjected to various displacement loading paths with loading-unloading cycles. The evolution of normal and tangential permeabilities predicted by the neural network are presented and are compared to the empirical Kozeny-Carman equation.
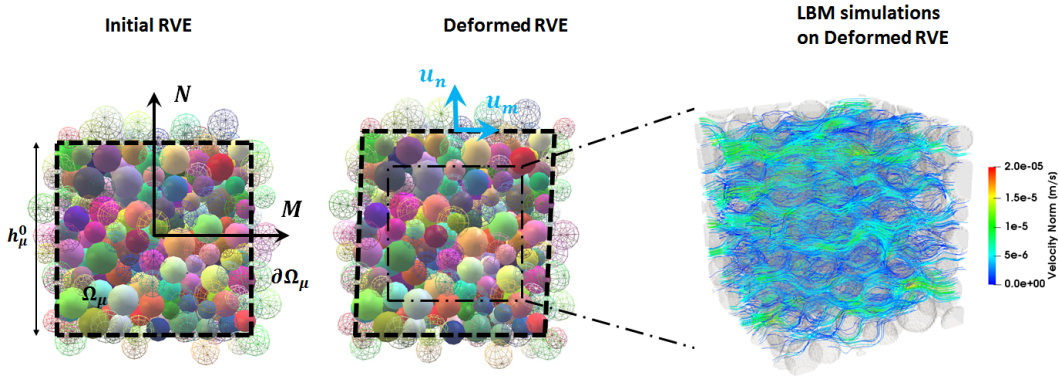

Fig. 2: Initial and deformed configurations of the particle assembly representing the granular materials inside strong discontinuity. The effective permeabilities in the normal and tangential directions are determined by Lattice-Boltzmann simulations on representative volume of current particle assembly.

The numerical solutions of Stokes equations using Lattice-Boltzmann method yield accurate results, especially in the low Reynold number regime, but require significant computational resources to resolve the flow field at pore space. To achieve a reasonable accuracy, the number of degree of freedoms required to obtain the effective permeability is at least a few orders more than those used in discrete element simulations [Sun et al., 2013] Thus, querying the effective permeability tensor from LBM simulations from each RVE for all incremental steps during a multiscale simulation is computationally expensive. In this work, we resort to a deep learning approach to predict the effective permeability for each incremental step. The design, training, and testing of the LSTM network on path-dependent material constitutive laws are detailed in a separate and dedicated work (cf. Wang and Sun [2018]). For completeness, a brief overview is provided.

First, a database containing the prescribed displacement jump loading paths, porosity and associated computed permeabilities is established by running multiple LBM simulations on deformed discrete element RVEs. Then, a recurrent neural network consisting of Long-Short-Term-Memory (LSTM) layers (see Figure 3) is trained using the database generated by LBM simulations [Hochreiter and Schmidhuber, 1997, Wang and Sun, 2017a]. In a nutshell, the training process attempts to minimize an objective function by adjusting the weights of each neuron in the layers through a back-propagation process. The LSTM approach is different than the traditional feed-forward neural network proposed by Ghaboussi et al. [1998] and Lefik and Schrefler [2002] in the sense that (1) the LSTM neuron (see Figure 4) has the capacity to use internal memory to process history and sequence and hence ideal for predictions for path-dependent materials, (2)
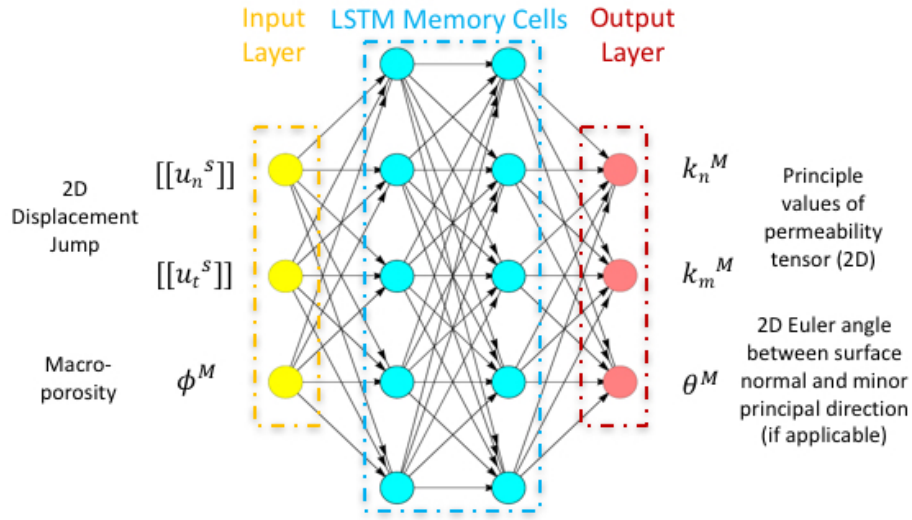
Fig. 3: The recurrent neural network used to predict the permeability of the interface.

the LSTM networks are designed to avoid a problem called vanishing or exploding gradient problems that may otherwise lead to issues during the training process.
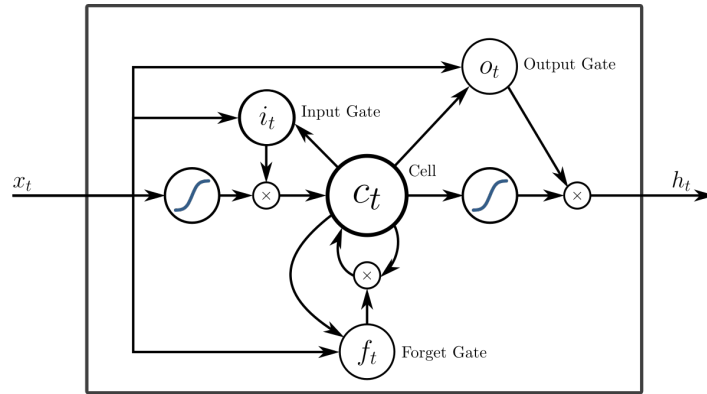

Fig. 4: A LSTM block with input, output and forget gates.

Finally, in each incremental update of the multiscale strong discontinuity simulation, the updated effective permeability components are generated by propagating signals from the input layer of the recurrent neural network to the output layers. In this particular case, the current displacement jumps and porosity are used as the input and the principal values and the spectral directions of the effective permeability tensor are the output of the recurrent neural network. One important upshot of this approach is that the querying time is largely reduced, as the deep learning permeability model typically requires only few seconds to make predictions.

Remarks on the computation time Each LBM simulation for determining the permeability of a DEM assembly costs a CPU time of 5 minutes. If the LBM simulation is used online with the FEM-DEM simulation, suppose there exist 10 000 integration points in a finite element mesh, for each iteration within each time step, the total CPU time spent in updating the permeability will be 50 000 minutes. If the data-driven approach is adopted, the LBM simulations are conducted offline to generate the database for the perme-
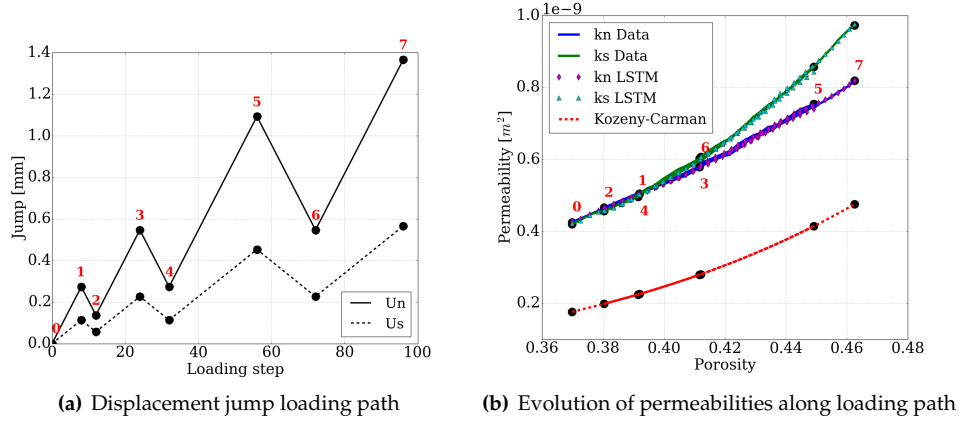
(a) Displacement jump loading path

(b) Evolution of permeabilities along loading path

Fig. 5: Example of permeability data generated from LBM simulations on RVEs undergoing loading-unloading sequences. (a) loading path of the normal Un and tangential displacement jumps Us. (b) Comparison between the normal kn and tangential ks permeability data from LBM simulations and the permeability components from predictions of LSTM neural network model. The calculation from empirical Kozeny-Carman equation $k = \frac{d_{50}^2}{180} \frac{\phi^3}{(1-\phi)^2}$ ($d_{50} = 1mm$) is shown for comparison.

ability of DEM assembly. The total CPU time is 5 000 minutes, when the overall size of the training and testing data is 1 000. The training and testing of a LSTM neural network model is 250 minutes. The CPU time for a LSTM neural network to predict permeability online with the FEM-DEM simulation is less than 1 minute for 10 000 integration points. Suppose a simulation consists of 100 time steps and each time step requires on average 10 iterations to converge. The comparison of CPU time spent on permeability calculation between the online approach and the data-driven approach is 50 000 000 (5 000 * 100 * 10) minutes against 6 250 (5 000 + 250 + 1*100*10) minutes. This justifies the advantage of artificial neural network over the online LBM simulations in saving the computation time.

4 Finite Element Implementation

The finite element formulation for porous continua with double porosity is detailed in Borja and Choo [2016]. This section presents the formulation for double-pore porous media incorporating assumed enhanced strain, following the Petrov-Galerkin multiscale formulation developed in [Borja, 2002, 2008] and the formulation for strong discontinuities in coupled porous media developed in [Callari and Armero, 2004]. In this work, constant strain triangle (CST) element is adopted, which simplifies the incorporation of the assumed enhanced strain (AES) in the finite element formulation. The displacement, macro- and micro-pressure fields are interpolated using the same linear shape functions. This type of low-order mixed finite element does not satisfy the inf-sup condition and can lead to pressure oscillations under undrained conditions. The pressure projection stabilization scheme is employed, as detailed in [Choo and Borja, 2015], although the weak forms presented herein do not contain these stabilization terms for brevity. Based on an alternative implementation of the AES modeling of strong discontinuity at finite strain [Mosler, 2006], we propose a novel framework that can conveniently and directly utilize the traction-separation law $T_\Gamma' = T_\Gamma'(\llbracket u \rrbracket)$ homogenized from micro-scale RVEs.

4.1 Weak form

Define the trial spaces of displacement, Cauchy macropore pressure and Cauchy micropore pressure as

$$
\begin{aligned}
\mathcal{S}_u &= \{ \boldsymbol{u} : \mathcal{B} \to \mathbb{R}^{n_{sd}} | \; \boldsymbol{u} \in H^1, \; \boldsymbol{u}|_{\partial B_u} = \hat{\boldsymbol{u}} \}, \\
\mathcal{S}_{p_M} &= \{ p_M : \mathcal{B} \to \mathbb{R} | \; p_M \in H^1, \; p_M|_{\partial B_{p_M}} = \hat{p}_M \}, \\
\mathcal{S}_{p_m} &= \{ p_m : \mathcal{B} \to \mathbb{R} | \; p_m \in H^1, \; p_m|_{\partial B_{p_m}} = \hat{p}_m \},
\end{aligned}
\tag{44}
$$

and the corresponding admissible spaces of variations as

$$
\begin{aligned}
\mathcal{V}_\eta &= \{ \boldsymbol{\eta} : \mathcal{B} \to \mathbb{R}^{n_{sd}} | \; \boldsymbol{\eta} \in H^1, \; \boldsymbol{\eta}|_{\partial B_u} = \boldsymbol{0} \}, \\
\mathcal{V}_{\zeta_M} &= \{ \zeta_M : \mathcal{B} \to \mathbb{R} | \; \zeta_M \in H^1, \; \zeta_M|_{\partial B_{p_M}} = 0 \}, \\
\mathcal{V}_{\zeta_m} &= \{ \zeta_m : \mathcal{B} \to \mathbb{R} | \; \zeta_m \in H^1, \; \zeta_m|_{\partial B_{p_m}} = 0 \},
\end{aligned}
\tag{45}
$$

where H^1 denotes the Sobolev space of functions of order one.

The variational form of the large-scale problem is constructed as: find $\boldsymbol{u} \in \mathcal{S}_u$, $p_M \in \mathcal{S}_{p_M}$ and $p_m \in \mathcal{S}_{p_m}$
such that for all $\boldsymbol{\eta} \in \mathcal{V}_\eta$, $\zeta_M \in \mathcal{V}_{\zeta_M}$ and $\zeta_m \in \mathcal{V}_{\zeta_m}$

$$
G \; : \; \mathcal{S}_u \times \mathcal{S}_{p_M} \times \mathcal{S}_{p_m} \times \mathcal{V}_\eta \to \mathbb{R}
$$
$$
G(\boldsymbol{u}, p_M, p_m, \boldsymbol{\eta}) = \int_{\mathcal{B}} \nabla^X \boldsymbol{\eta} : \boldsymbol{P} \, dV - \int_{\mathcal{B}} \boldsymbol{\eta} \cdot \rho_0 \boldsymbol{g} \, dV + \int_{\mathcal{B}} \boldsymbol{\eta} \cdot c_0 (\widetilde{\boldsymbol{v}}_m - \widetilde{\boldsymbol{v}}_M) \, dV - \int_{\partial \mathcal{B}_t} \boldsymbol{\eta} \cdot \hat{\boldsymbol{t}} \, dA = 0
\tag{46}
$$

$$
H_{p_M} \; : \; \mathcal{S}_u \times \mathcal{S}_{p_M} \times \mathcal{S}_{p_m} \times \mathcal{V}_{\zeta_M} \to \mathbb{R}
$$
$$
H_{p_M}(\boldsymbol{u}, p_M, p_m, \zeta_M) = \int_{\mathcal{B}} \zeta_M \, \dot{\rho}_0^M \, dV - \int_{\mathcal{B}} \nabla^X \zeta_M \cdot \boldsymbol{Q}_M \, dV + \int_{\mathcal{B}} \zeta_M \, c_0 \, dV - \int_{\partial \mathcal{B}_{q_M}} \zeta_M \, \hat{Q}_M \, dA = 0
\tag{47}
$$

$$
H_{p_m} \; : \; \mathcal{S}_u \times \mathcal{S}_{p_M} \times \mathcal{S}_{p_m} \times \mathcal{V}_{\zeta_m} \to \mathbb{R}
$$
$$
H_{p_m}(\boldsymbol{u}, p_M, p_m, \zeta_m) = \int_{\mathcal{B}} \zeta_m \, \dot{\rho}_0^m \, dV - \int_{\mathcal{B}} \nabla^X \zeta_m \cdot \boldsymbol{Q}_m \, dV - \int_{\mathcal{B}} \zeta_m \, c_0 \, dV - \int_{\partial \mathcal{B}_{q_m}} \zeta_m \, \hat{Q}_m \, dA = 0
\tag{48}
$$

Applying the effective stress principle Eq. (13), the internal virtual work term in Eq. (46) can be written
in spatial form as,

$$
\begin{aligned}
\int_{\mathcal{B}} \nabla^X \boldsymbol{\eta} : \boldsymbol{P} \, dV &= \int_{\mathcal{B}} \nabla^X \boldsymbol{\eta} : \boldsymbol{\tau} \cdot \overline{\boldsymbol{F}}^{-T} \, dV \\
&= \int_{\mathcal{B}} \nabla^{\overline{x}} \boldsymbol{\eta} : \boldsymbol{\tau} \, dV \\
&= \int_{\mathcal{B}} \nabla^{\overline{x}} \boldsymbol{\eta} : (\boldsymbol{\tau}' - \overline{J} p^{\mathrm{avg}} \boldsymbol{I}) \, dV,
\end{aligned}
\tag{49}
$$

where $\nabla^{\overline{x}} \boldsymbol{\eta} = \partial \boldsymbol{\eta} / \partial \overline{x}$ and $\overline{J} = \det(\overline{\boldsymbol{F}})$.

Combining the equations (7), (8), (49) and using the backward Euler implicit scheme of step size $\Delta t = $
$t_{n+1} - t_n$, the time-integrated spatial form of the variational equations (46), (47), (48) become

$$
\begin{aligned}
G(\boldsymbol{u}, p_M, p_m, \boldsymbol{\eta}) = \underbrace{\int_{\mathcal{B}} \nabla^{\overline{x}} \boldsymbol{\eta} : \boldsymbol{\tau}' \, dV}_{g_1} - \underbrace{\int_{\mathcal{B}} \nabla^{\overline{x}} \cdot \boldsymbol{\eta} \, \overline{J} p^{\mathrm{avg}} \, dV}_{g_2} \\
- \underbrace{\int_{\mathcal{B}} \boldsymbol{\eta} \cdot \rho_0 \boldsymbol{g} \, dV}_{g_3} + \underbrace{\int_{\mathcal{B}} \boldsymbol{\eta} \cdot c_0 (\widetilde{\boldsymbol{v}}_m - \widetilde{\boldsymbol{v}}_M) \, dV}_{g_4} - \underbrace{\int_{\partial \mathcal{B}_t} \boldsymbol{\eta} \cdot \hat{\boldsymbol{t}} \, dA}_{g_{ext}} = 0
\end{aligned}
\tag{50}
$$

$$H_{p_M}^{\Delta t}(\boldsymbol{u}, p_M, p_m, \zeta_M) = \underbrace{\int_{\mathcal{B}} \zeta_M \, (\rho_0^M - \rho_{0_n}^M) \, dV}_{h_1^M}$$

$$\underbrace{+\Delta t \, \rho_f \int_{\mathcal{B}} \nabla^x \zeta_M \cdot J \, \frac{\boldsymbol{k}_M}{\mu_f} \cdot (\nabla^x p_M - \rho_f \boldsymbol{g}) \, dV}_{h_2^M} \qquad (51)$$

$$\underbrace{+\Delta t \int_{\mathcal{B}} \zeta_M \, c_0 \, dV}_{h_3^M} - \underbrace{\Delta t \int_{\partial \mathcal{B}_{q_M}} \zeta_M \, \hat{Q}_M \, dA}_{h_{ext}^M} = 0$$

$$H_{p_m}^{\Delta t}(\boldsymbol{u}, p_M, p_m, \zeta_m) = \underbrace{\int_{\mathcal{B}} \zeta_m \, (\rho_0^m - \rho_{0_n}^m) \, dV}_{h_1^m}$$

$$\underbrace{+\Delta t \, \rho_f \int_{\mathcal{B}} \nabla^x \zeta_m \cdot J \, \frac{\boldsymbol{k}_m}{\mu_f} \cdot (\nabla^x p_m - \rho_f \boldsymbol{g}) \, dV}_{h_2^m} \qquad (52)$$

$$\underbrace{-\Delta t \int_{\mathcal{B}} \zeta_m \, c_0 \, dV}_{h_3^m} - \underbrace{\Delta t \int_{\partial \mathcal{B}_{q_m}} \zeta_m \, \hat{Q}_m \, dA}_{h_{ext}^m} = 0$$

4.2 Traction continuity in assumed enhanced constant strain triangle element

For an AES CST element $\mathcal{B}_X^e$ adopted in the simulations, the stress $\boldsymbol{P}'$, normal $\boldsymbol{N}$ and traction $\boldsymbol{T}'_\Gamma$ are uniform inside the element. Thus the local equilibrium equation (24) holds in $\mathcal{B}_X^e$ as the residual form:

$$\boldsymbol{r} = \boldsymbol{P}'(\overline{\boldsymbol{F}}) \cdot \boldsymbol{N} - \boldsymbol{T}'_\Gamma([\![\boldsymbol{u}]\!]) = \boldsymbol{0} \qquad (53)$$

The variation of the residual writes

$$\delta \boldsymbol{r} = \delta(\boldsymbol{\tau}' \cdot \overline{\boldsymbol{F}}^{-T} \cdot \boldsymbol{N}) - \delta \boldsymbol{T}'_\Gamma$$
$$= (\delta \boldsymbol{\tau}' \cdot \overline{\boldsymbol{F}}^{-T} + \boldsymbol{\tau}' \cdot \delta \overline{\boldsymbol{F}}^{-T}) \cdot \boldsymbol{N} - \delta \boldsymbol{T}'_\Gamma. \qquad (54)$$

Recall the linearization of $\boldsymbol{\tau}'$ as, if the host continuum assumes a hyperelastic constitutive law,

$$\delta \boldsymbol{\tau}' = \boldsymbol{\alpha}^e : \nabla^{\overline{x}} \delta \overline{\boldsymbol{u}}, \qquad (55)$$

and the linearization of $\overline{\boldsymbol{F}}^{-1}$ as

$$\delta \overline{\boldsymbol{F}}^{-1} = -\overline{\boldsymbol{F}}^{-1} \cdot \nabla^{\overline{x}} \delta \overline{\boldsymbol{u}}, \qquad (56)$$

and that

$$\nabla^{\overline{x}} \delta \overline{\boldsymbol{u}} = \delta \overline{\boldsymbol{F}} \cdot \overline{\boldsymbol{F}}^{-1}, \qquad (57)$$
$$\nabla^x \delta \boldsymbol{u} = \delta \boldsymbol{F} \cdot \boldsymbol{F}^{-1}. \qquad (58)$$

Inserting Eq. (55), (56) and (57) into Eq. (54),

$$\delta \boldsymbol{r} = (\boldsymbol{\alpha}^e : \nabla^{\overline{x}} \delta \overline{\boldsymbol{u}} \cdot \overline{\boldsymbol{F}}^{-T} - \boldsymbol{\tau}' \cdot (\nabla^{\overline{x}} \delta \overline{\boldsymbol{u}})^T \cdot \overline{\boldsymbol{F}}^{-T}) \cdot \boldsymbol{N} - \delta \boldsymbol{T}'_\Gamma$$
$$= (\boldsymbol{\alpha}^e - \boldsymbol{\tau}' \ominus \boldsymbol{I}) : (\delta \overline{\boldsymbol{F}} \cdot \overline{\boldsymbol{F}}^{-1}) \cdot \overline{\boldsymbol{F}}^{-T} \cdot \boldsymbol{N} - \delta \boldsymbol{T}'_\Gamma$$
$$\Rightarrow \quad \delta r_i = \underbrace{(\boldsymbol{\alpha}^e - \boldsymbol{\tau}' \ominus \boldsymbol{I})_{ijkl} (\boldsymbol{I}^4)_{kmnp} \overline{F}_{ml}^{-1} \overline{F}_{qj}^{-1} N_q}_{\mathbb{A}_{inp}} \delta \overline{F}_{np} - \delta T'_{\Gamma i} \qquad (59)$$

$$\Rightarrow \quad \delta \boldsymbol{r} = \mathbb{A} : \delta \overline{\boldsymbol{F}} - \delta \boldsymbol{T}'_\Gamma.$$

From Eq. 18, the linearization of $\overline{F}$ is given by:

$$\delta\overline{F} = \delta F - \delta\, [\![u]\!] \otimes \nabla^X f_\mathcal{S}$$
$$= \delta F - \mathbb{T} \cdot \delta\, [\![u]\!], \tag{60}$$

with $\mathbb{T}$ defined as $(\mathbb{T})_{ijk} = \delta_{ik}(\nabla^X f_\mathcal{S})_j$.

In the local solution of the traction continuity equation (53), the conformal deformation gradient F is predetermined by the solution of the equilibrium equations of the large-scale problem, thus $\delta F = 0$, and then the Jacobian to be used in the local iterative solution is given by

$$\delta r = \underbrace{(-\mathbb{A} : \mathbb{T} - \frac{\partial T'_\Gamma}{\partial\, [\![u]\!]})}_{\mathscr{D}} \cdot \delta\, [\![u]\!]. \tag{61}$$

At the converged state of local equilibrium equation (53), $\delta r = 0$, thus, combining Eq. (59) and (60),

$$\delta r = \mathbb{A} : \delta F + \mathscr{D} \cdot \delta\, [\![u]\!] = 0$$
$$\Rightarrow \quad \delta\, [\![u]\!] = -\mathscr{D}^{-1} \cdot \mathbb{A} : \delta F. \tag{62}$$

For Petrov-Galerkin finite element formulation involving AES, the gradient of the variation function is evaluated over the continuous part of the deformation map, whereas the gradient of the trial function is evaluated over the conforming part of the deformation map. According to Eq. (57), (58), (60) and (62), we establish the relationships between these two gradients

$$\nabla^{\overline{x}}\delta\overline{u} = (\delta F - \mathbb{T} \cdot \delta\, [\![u]\!]) \cdot \overline{F}^{-1}$$
$$= (I^4 + \mathbb{T} \cdot \mathscr{D}^{-1} \cdot \mathbb{A}) : \delta F \cdot \overline{F}^{-1}$$
$$= (I^4 + \mathbb{T} \cdot \mathscr{D}^{-1} \cdot \mathbb{A}) : (\nabla^x \delta u \cdot F) \cdot \overline{F}^{-1}$$
$$\Rightarrow \quad (\nabla^{\overline{x}}\delta\overline{u})_{ij} = \underbrace{[(I^4)_{impq} + (\mathbb{T})_{imr}(\mathscr{D}^{-1})_{rs}(\mathbb{A})_{spq}](I^4)_{pqkl}F_{mn}\overline{F}^{-1}_{nj}}_{\mathscr{A}_{ijkl}}(\nabla^x\delta u)_{kl}$$
$$\Rightarrow \quad \nabla^{\overline{x}}\delta\overline{u} = \mathscr{A} : \nabla^x \delta u. \tag{63}$$

4.3 Consistent linearization of the finite strain AES double-porosity formulation

Due to the diffusion-deformation coupling and the coupling between the pore-fluid diffusion in the macro-pores and the micro-pores, an unconditionally stable time integration algorithm is used to numerically solve the multiscale problem. As a result, a consistent tangent is needed for obtaining the numerical solution via iterative methods. In this derivation, we assumed that a monolithic solver is used and there is no operator split applied. Previous work such as Wollny et al. [2017] has explored the usage of split operator for finite strain poromechanics based on the relevant work on the small strain counterparts (e.g. Armero and Callari [1999], Kim et al. [2011], Mikelić and Wheeler [2013]. As explained in Wollny et al. [2017], the expression of the tangential operator for the operator-split algorithm would be different, depending on which term(s) is frozen for each split step. Comparisons between the monolithic and operator-split approach is out of the scope of the current study but will be considered in the future.

For the linearization of the weak form of the linear momentum conservation equation (50), since the terms g_1 and g_2 involve both continuous and conformal deformation, equations in the previous subsection on local traction continuity are employed. Using Eq. (55), (56), (63) and identities $\delta\nabla^{\overline{x}}\eta = -\nabla^{\overline{x}}\eta \cdot \nabla^{\overline{x}}\delta\overline{u}$, $\delta\overline{J} = \overline{J}\nabla^{\overline{x}}\cdot\delta\overline{u}$,

$$\delta g_1 = \int_\mathcal{B} \nabla^{\overline{x}}\eta : (\alpha^e - \tau' \ominus I) : \nabla^{\overline{x}}\delta\overline{u}\, dV$$
$$= \int_\mathcal{B} \nabla^{\overline{x}}\eta : [(\alpha^e - \tau' \ominus I) : \mathscr{A}] : \nabla^x \delta u\, dV, \tag{64}$$

$$
\begin{aligned}
\delta g_2 = & -\int_{\mathcal{B}} \delta(\nabla^{\bar{x}} \cdot \boldsymbol{\eta}) \, \bar{J} \, p^{\mathrm{avg}} \, dV - \int_{\mathcal{B}} \nabla^{\bar{x}} \cdot \boldsymbol{\eta} \, \delta\bar{J} \, p^{\mathrm{avg}} \, dV - \int_{\mathcal{B}} \nabla^{\bar{x}} \cdot \boldsymbol{\eta} \, \bar{J} \, \delta p^{\mathrm{avg}} \, dV \\
= & + \int_{\mathcal{B}} \nabla^{\bar{x}} \boldsymbol{\eta} : [\bar{J} \, p^{\mathrm{avg}} \, (\boldsymbol{I} \ominus \boldsymbol{I}) : \mathscr{A}] : \nabla^{x} \delta \boldsymbol{u} \, dV \\
& - \int_{\mathcal{B}} \nabla^{\bar{x}} \boldsymbol{\eta} : [\bar{J} \, p^{\mathrm{avg}} \, (\boldsymbol{I} \otimes \boldsymbol{I}) : \mathscr{A}] : \nabla^{x} \delta \boldsymbol{u} \, dV \\
& - \int_{\mathcal{B}} \nabla^{\bar{x}} \cdot \boldsymbol{\eta} \, \bar{J} \left[(p_M - p_m) \frac{\partial \psi}{\partial \boldsymbol{u}} \delta \boldsymbol{u} + \psi \, \delta p_M + (1 - \psi) \, \delta p_m \right] dV
\end{aligned}
\tag{65}
$$

The linearizations of the remaining terms of the weak forms (50), (51), (52) are identical to the large-scale double-porosity problem without AES, as they only involve conformal deformation. The formulae are grouped in Appendix A.

5 Numerical Examples

5.1 Mixed-mode shear tests on porous media with pre-existing interfaces

The proposed hydro-mechanical AES-DEM framework can model complex path-dependent interface behavior inside pre-existing fractures. This is illustrated in this section via mixed-mode shear tests on porous media specimen with embedded strong discontinuity (Fig. 6). The sample is 0.1 m x 0.1 m in dimension. The bottom edge is fixed, while the top edge moves rigidly along prescribed displacement path. The sample is assumed periodic in the horizontal direction, thus periodic displacement boundary condition is applied on the lateral edges. Water pressure in both macropores and micropores on the top and bottom edges are set to zero, representing drained surfaces. Two types of interface geometry are tested in this example. One is a horizontal straight line in the center and another is a sinusoid with the spatial period of 0.05 m and amplitude of 0.005 m. The sinusoidal shape mimics a rough surface in-between a bulk material.

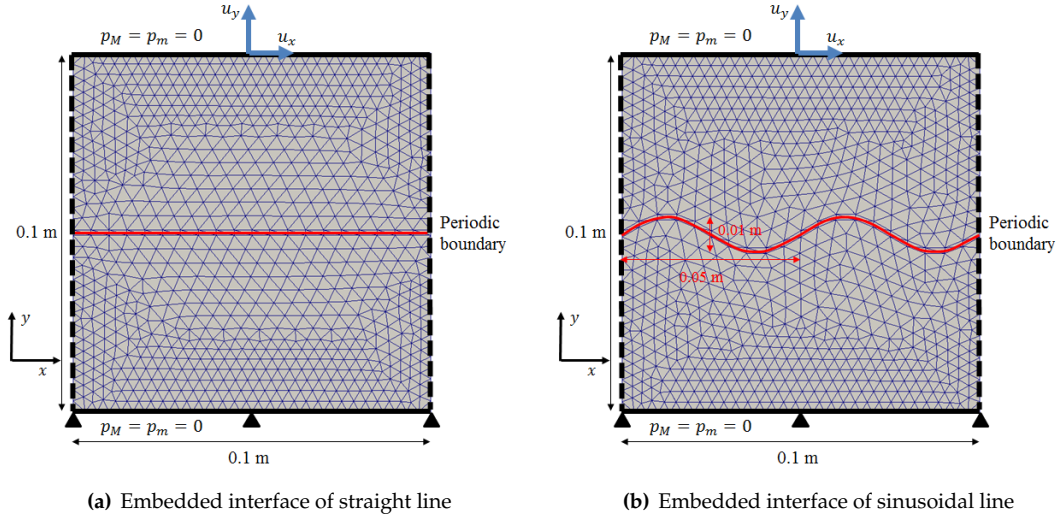**(a)** Embedded interface of straight line   **(b)** Embedded interface of sinusoidal line

Fig. 6: Geometry of fractured specimen and boundary conditions.

The mechanical and permeability properties of the interfaces are homogenized from the discrete element samples. The cohesive-frictional material for rock in YADE is adopted [Scholtès and Donzé, 2012, 2013]. The bulk material is idealized as isotropic hyperelastic material. The permeability tensors in macro-

Scale & Model	Location	Parameter	Value
Grain-scale DEM	micro-discontinuities	Particle Young's modulus E	0.1 GPa
Grain-scale DEM	micro-discontinuities	Particle Poisson's ratio ν	0.35
Grain-scale DEM	micro-discontinuities	Particle Friction Angle φ	$\frac{\pi}{6}$
Grain-scale DEM	micro-discontinuities	Particle density	2600 kg/m^3
Grain-scale DEM	micro-discontinuities	Particle mean diameter	5 mm
Grain-scale DEM	micro-discontinuities	Tensile strength T	5 MPa
Grain-scale DEM	micro-discontinuities	Local Cohesion C	5 MPa
Grain-scale DEM	micro-discontinuities	Interaction range γ_{int}	1.6
Grain-scale DEM	micro-discontinuities	Confining pressure	0 Pa
Grain-scale DEM-LBM	micro-discontinuities	Initial intrinsic permeability	$9e^{-10}$ m^2
Macro-scale FEM	macro-scale host matrix	Young's modulus E	0.2 GPa
Macro-scale FEM	macro-scale host matrix	Poisson's ratio ν	0.2
Macro-scale FEM	macro-scale host matrix	Porosity of macropore ϕ_M	0.05
Macro-scale FEM	macro-scale host matrix	Porosity of micropore ϕ_m	0.1
Macro-scale FEM	macro-scale host matrix	Intrinsic permeability of macropore k_M	$1e^{-10}$ m^2
Macro-scale FEM	macro-scale host matrix	Intrinsic permeability of micropore k_m	$1e^{-14}$ m^2
Macro-scale FEM	macro-scale host matrix	Parameter of mass transfer $\bar{\alpha}$	$100 * \rho_f * k_m$
Macro-scale FEM	macro-scale host matrix	Dynamic viscosity μ	$1e^{-3}$ Pa $\cdot$ s

Table 1: Material parameters for the grain- and macro-scale poromechanics problem with embedded strong discontinuities across length scales. The parameters for the cohesive-frictional DEM model for rock are defined in [Scholtès and Donzé, 2013].

and micro- pores of the bulk are assumed isotropic. The macropores in the bulk material refer to small fissures distributed homogeneously inside the porous media. The material parameters are presented in Table 1. The DEM assembly represents the material inside the fault gouge and the macro-scale Young's modulus for FEM is for the intact host continuum outside the fault. Nevertheless, the material parameters used for the DEM simulations are not suitable to represent the fault gouge composed of non—cohesive granular materials. These material parameters are merely chosen to create a benchmark case where the finite strain data-driven LBM-DEM-FEM framework can be completed within a limited amount of CPU time budgeted for the DEM simulations. Recall that the critical time step for explicit dynamic simulations in the DEM is related to the stiffness of the grain contacts. Higher stiffness generally leads to smaller critical time step and hence it takes longer to establish the static equilibrium [Liu et al., 2015, Wang and Sun, 2016a]. A more realistic set of material parameters for discrete element modeling of fault gouge can be found in the literature, such as Guo and Morgan [2007] in which the particle Young's modulus is about 70 GPa.

To prepare the DEM assembly for the multiscale simulations, we first conducted isotropic compression and simple shear simulations to recover the macroscopic bulk modulus and shear modulus of the grain assembly where the grain material parameters are shown in Table 1. We found that the macroscopic bulk modulus K of the DEM assembly is 84.0 MPa (inferred from the isotropic tension and compression tests) and the shear modulus G is 71.4 MPa (inferred from simple shear tests). In other words, the macroscopic Young's modulus of the assembly is 167 MPa and the Poisson's ratio is 0.17. This somewhat surprising result indicates that the use of bonded cohesive-frictional contact models for the DEM assembly, may lead to the effective Young's modulus higher than that of the particle. This can be attributed to the introduction of bonds among particles that lead to additional stiffness. As such, the materials in the embedded discontinuities exhibit only slightly lower macroscopic Young's modulus than that of the intact continuum and the difference is within the size of a round-off error.

Firstly, we examine the influence of infinitesimal strain formulation and finite strain formulation on the global stress-strain behavior of the numerical tests. The specimen with a straight interface is stretched and sheared at the same time, with a tension rate of 0.00005 m/s and a shear rate of 0.00004 m/s. The comparison of normal and shear stress-strain curves indicates a significant discrepancy in the peak stress

and softening regime between the two formulations (Fig. 7). This indicates that incorporating the geometrical nonlinearity is necessary for accurately predicting the interface behavior in the finite deformation regime. Secondly, we investigate the influence of the size of the assumed enhanced strain element with double porosity. Note that in the current formulation, the standard integration is adopted in the finite elements embedding the strong discontinuity for both macropore and micropore fluid flow fields, hence the fluid flow solutions are dependent on the sizes of the traced finite elements. In order to accurately capture the fluid flows in the neighborhood of the faults, such traced elements should have small heights and are aligned with the fault interfaces. The height of the element in the coarse mesh is 0.0015 m, and it is downsized to 0.0005 m in the fine mesh. Fig. 8 presents the curves of stress on the top surface vs. strain of the specimen in the normal (y) and shear (x) directions using both meshes. The dependency of solutions on mesh size is not significant when the elements with embedded strong discontinuity are aligned with the pre-existing interface and have small element heights. The effect of element orientation is not studied, since, in this work, the AES elements are always in alignment with the geometry of the pre-existing fractures.

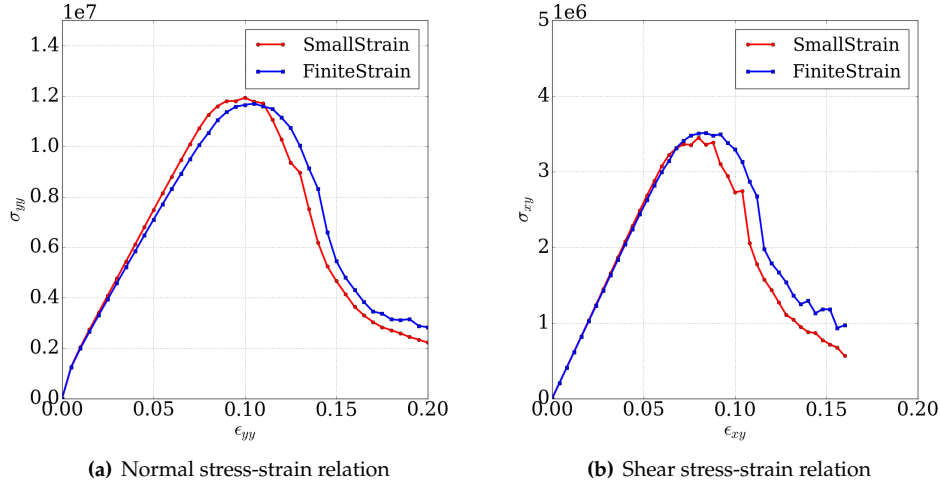**(a)** Normal stress-strain relation   **(b)** Shear stress-strain relation

Fig. 7: Comparison of small strain and finite strain AES-DEM formulations for mixed-shear test on the specimen with straight interface.

Next, we present the effect of interface geometry (embedded straight interface and sinusoidal interface Fig. 6). A mixed-mode loading-unloading-reloading path is applied on the top surface of the specimens. The time history of the deformation is plotted in Fig. 9. The global stress-strain curves in normal and shear directions are compared. Because of a high surface roughness for the sinusoidal interface, it can sustain higher shear stress compared to the straight interface, in both peak and softening regime. The differential stress and strain fields at the final stage of the loading are shown in Fig. 10. The strain localizes in the embedded strong discontinuity in both specimens. The stress field exhibits a homogeneous distribution for straight interface, while a stress concentration pattern exists in the specimen with the sinusoidal interface.

Due to the fully coupled nature of the problem, the pore pressure and fluid flow inside the specimens strongly depend on the opening and shear of the strong discontinuity. The field of pore pressure and fluid flux in macropores presented in Fig. 11 show the motion of water from small fissures in bulk material into the enlarged pore space in the embedded strong discontinuity. The opening and the plastic dilatancy due to shearing of the pre-existing fracture result in the increase of effective permeability of the macropore space in the elements with embedded strong discontinuity. There is also fluid flow inside the channel in the interface whose permeability is enhanced by . For micropores, the distributions of pore pressure and flux in Fig. 11 also suggest the motion of water from surrounding bulk material to the solid matrix containing the interface.
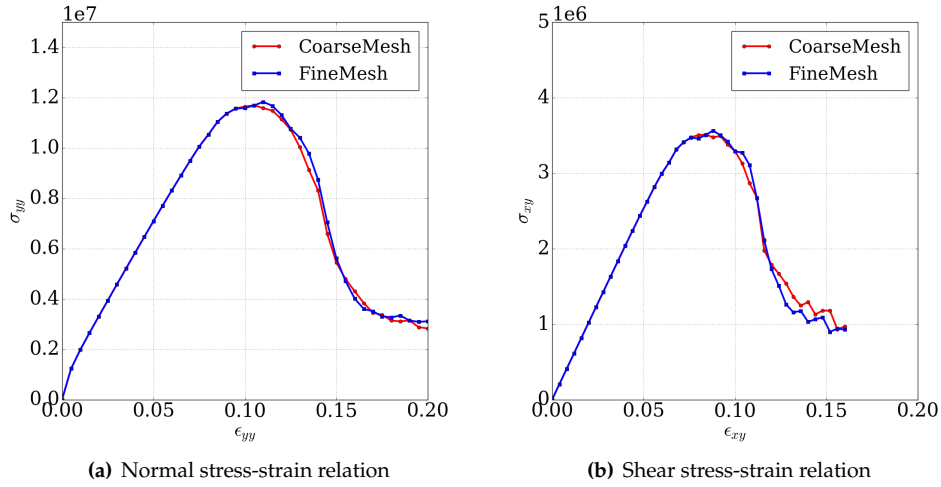
(a) Normal stress-strain relation

(b) Shear stress-strain relation

Fig. 8: Comparison of global stress-strain behavior with coarse mesh and fine mesh for mixed-shear test on the specimen with straight interface.
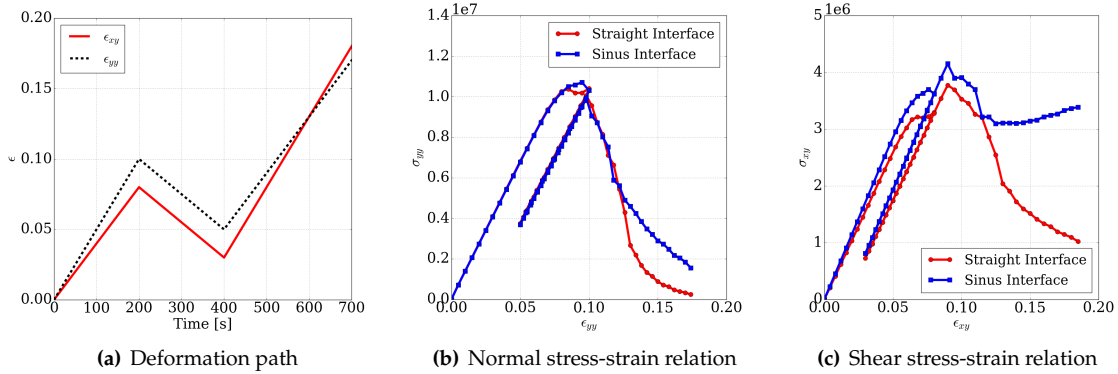

(a) Deformation path

(b) Normal stress-strain relation

(c) Shear stress-strain relation

Fig. 9: Influence of interface geometry on the global stress-strain behavior in mixed-mode shear tests

5.2 Reactivation of faults

This example analyzes the slip of a pre-existing and formerly stable fault in saturated soil triggered by the injection of water at a nearby location. The idealized problem geometry and boundary conditions are shown in Fig. 12. The dimensions of the 2D field of saturated porous media are 10 m x 10 m. The domain is constrained in the x-direction on the left boundary and in the y-direction on the bottom boundary. A foundation has been constructed on top of the domain, generating a uniform loading pressure of 10 MPa. A lateral confining pressure of 5 MPa is applied on the right boundary for the frictional porous media to sustain the vertical load. There exists a 45-degree fault under the foundation. The entire system is stable and has been in equilibrium for a long time since the construction of the foundation, thus the excess pore pressures in both fractures and host matrix are zero. The initial effective stress of the porous solid is hence

$$\sigma'_{\text{Init}} = \begin{bmatrix} -5 & 0 \\ 0 & -10 \end{bmatrix}_{xy} \text{MPa}, \tag{66}$$

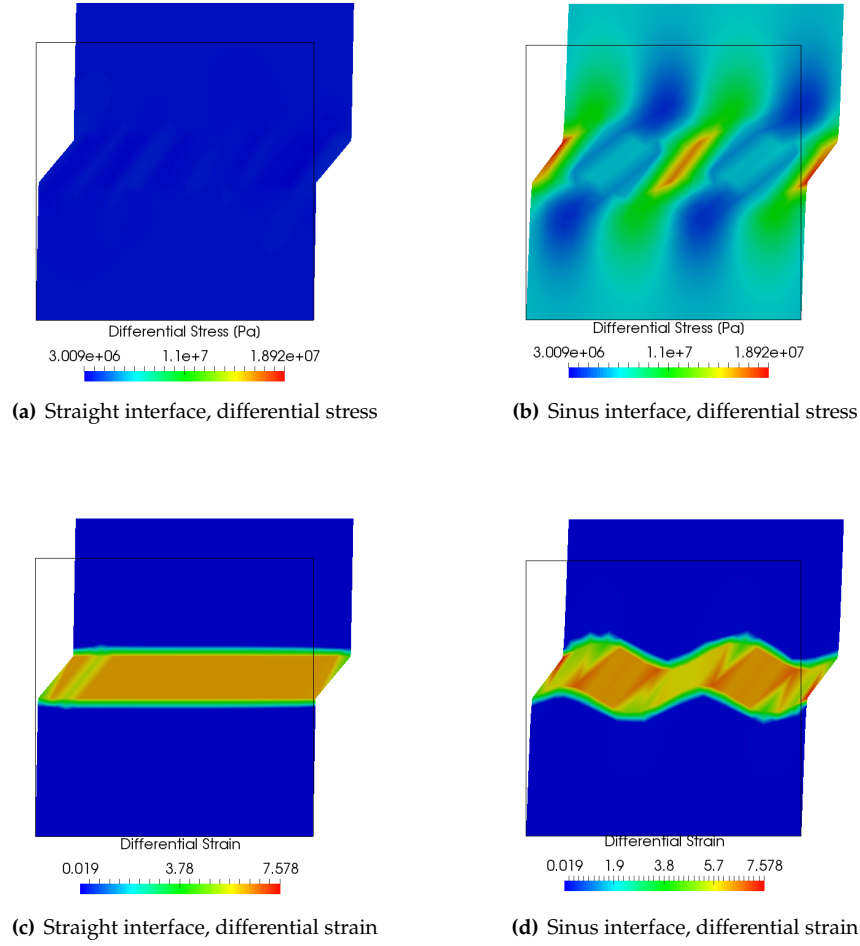where the subscript xy refers to the coordinate system $\{x, y\}$ depicted in Fig. 12.

(a) Straight interface, differential stress

(b) Sinus interface, differential stress

(c) Straight interface, differential strain

(d) Sinus interface, differential strain

Fig. 10: Influence of interface geometry on the differential stress field ($\tau_1 - \tau_3$, where τ_1 is the greatest principal value and τ_3 is the least principal value of the Kirchhoff stress tensor $\boldsymbol{\tau}$) and the differential strain field ($b_1 - b_3$, where b_1 is the greatest principal value and b_3 is the least principal value of the Left Cauchy-Green deformation tensor $\boldsymbol{b}$) in mixed-mode shear tests.

The DEM RVEs characterizing the traction-separation law of the fault are placed in alignment with the strong discontinuity. They must be in the initial stress state consistent to the macroscopic boundary conditions. From the initial stress state of the macro-scale problem (Eq. 66) and via a coordinate transformation ($\sigma^{mn} = \boldsymbol{R}^{\mathrm{T}} \cdot \sigma^{xy} \cdot \boldsymbol{R}$), the initial stress tensor of the DEM assemblies is expressed as

$$\sigma'_{\mathrm{InitRVE}} = \begin{bmatrix} -7.5 & 2.5 \\ 2.5 & -7.5 \end{bmatrix}_{mn} \mathrm{MPa}, \tag{67}$$

where the subscript mn refers to the rotated frame $\{m, n\}$ for the fault depicted in Fig. 12. The initial DEM RVEs in this stress state provide the correct amount of initial shear and normal tractions along the strong discontinuity.

In this example, the particle contact model for DEM is frictional and without cohesion. The normal and tangential permeabilities are obtained from machine learning models trained with LBM simulation data. The bulk material is idealized as isotropic hyperelastic material. The permeability tensors in macro- and

(a) Straight interface, pressure and flow in macropore **(b)** Sinus interface, pressure and flow in macropore

(c) Straight interface, pressure and flow in micropore **(d)** Sinus interface, pressure and flow in micropore
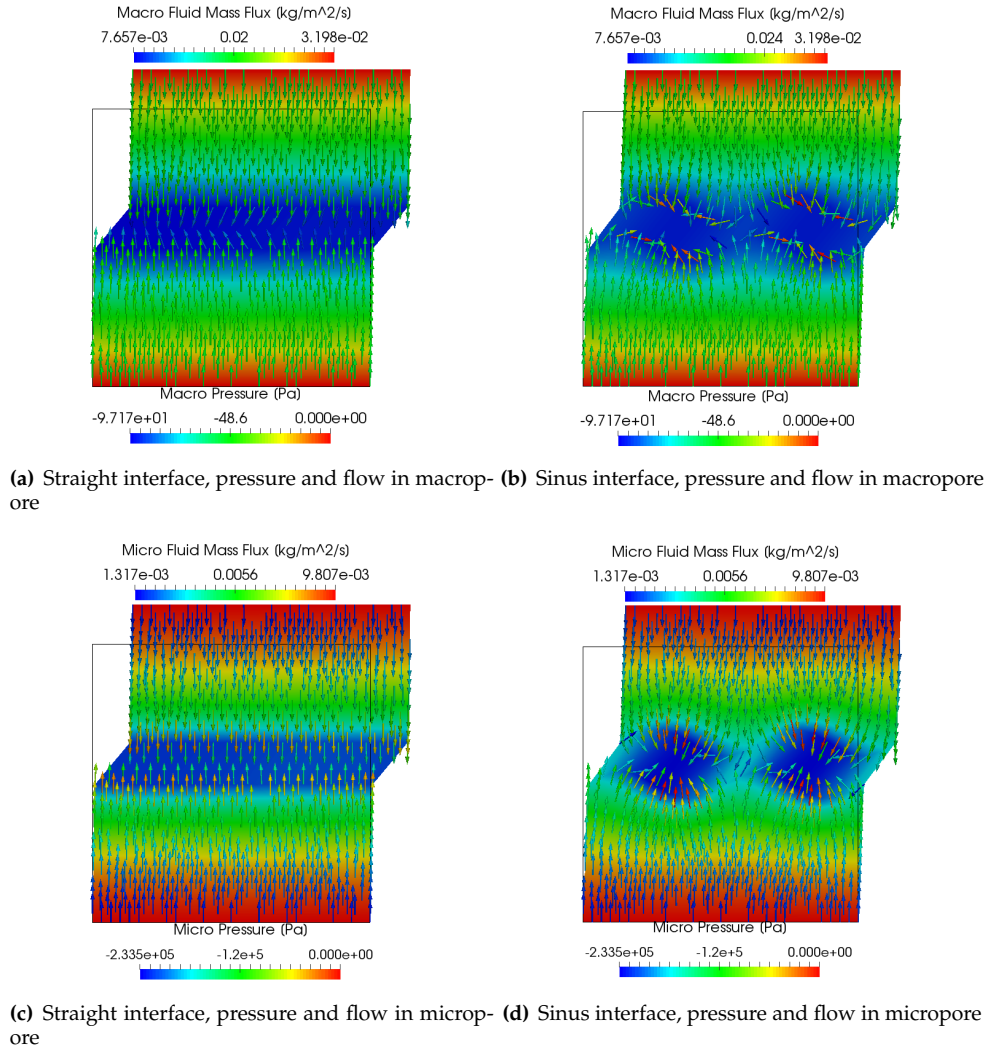
Fig. 11: Influence of interface geometry on the macropore and micropore pressure fields in mixed-mode shear tests

micro-pores of the bulk are assumed isotropic and evolve according to the Kozeny-Carman equation. The material parameters used in the numerical example are summarized in Table 2.

Water is injected to the macropore space (pre-existing fractures) of the field through the source S located at the center of the domain. The macropore pressure is zero on the top surface and the other three surfaces are no-flow boundaries. There is no drainage boundary for micropore pressure. This flow boundary condition is to suppress spurious micropore pressure oscillations near the drainage boundary [Choo and Borja, 2015]. The prescribed time history of Darcy velocity at the source is shown in Fig. 13. The injection profile is composed of injection-pause cycles, in which water supply is provided for 40 hours under a constant rate of 0.02 m/s, followed by a pause for 10 hours before the next cycle of injection. From the simulation results, the time history of the pore pressure in both scales at the source S is presented in Fig. 13. Upon injection or pause, the macropore injection pressure jumps up or plunges immediately, while the micropore pressure at the injection point has the opposite behavior. This is caused by the low mass transfer permeability between the macropores and micropores. Then in the transient regime, when fluid gradually diffuses into
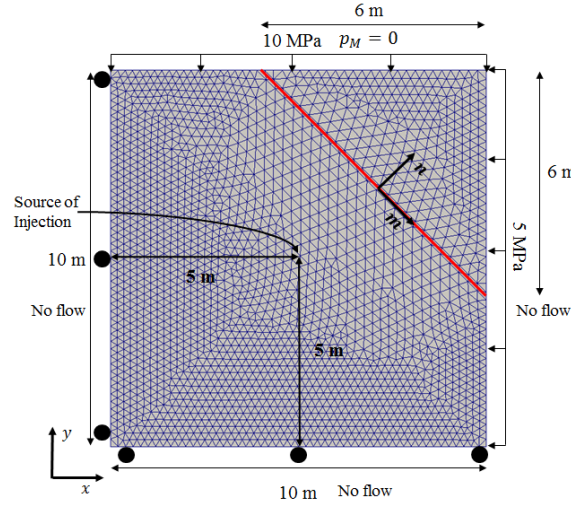
Fig. 12: Geometry of fault reactivation problem and boundary conditions. Red line represents the pre-existing fault.

Scale & Model	Location	Parameter	Value
Grain-scale DEM	micro-discontinuities	Particle Young's modulus E	0.5 GPa
Grain-scale DEM	micro-discontinuities	Particle Poisson's ratio ν	0.3
Grain-scale DEM	micro-discontinuities	Particle Friction Angle φ	$\frac{\pi}{6}$
Grain-scale DEM	micro-discontinuities	Particle density	2600 kg/m^3
Grain-scale DEM	micro-discontinuities	Particle mean diameter	0.5 mm
Grain-scale DEM-LBM	micro-discontinuities	Initial intrinsic permeability	$9e^{-14}$ m^2
Macro-scale FEM	macro-scale host matrix	Young's modulus E	0.2 GPa
Macro-scale FEM	macro-scale host matrix	Poisson's ratio ν	0.2
Macro-scale FEM	macro-scale host matrix	Porosity of macropore ϕ_M	0.05
Macro-scale FEM	macro-scale host matrix	Porosity of micropore ϕ_m	0.1
Macro-scale FEM	macro-scale host matrix	Intrinsic permeability of macropore k_M	$1e^{-14}$ m^2
Macro-scale FEM	macro-scale host matrix	Intrinsic permeability of micropore k_m	$1e^{-17}$ m^2
Macro-scale FEM	macro-scale host matrix	Parameter of mass transfer $\bar{\alpha}$	$\rho_f * k_m$
Macro-scale FEM	macro-scale host matrix	Dynamic viscosity μ	$1e^{-3}$ Pa · s

Table 2: Material parameters for the grain- and macro-scale poromechanics problem with embedded strong discontinuities across length scales. The parameters for the simple frictional DEM model are defined in [Šmilauer and Chareyre, 2015].

the micropores by mass transfer, micropore pressure slowly approaches the macropore pressure. The two pressures will eventually be identical when the diffusion between pores reaches equilibrium.

The macropore and micropore pressure field at time 40 h, 100 h and 180 h are presented in Fig. 14. The pressure plume is initially of the shape of a circle and then expands as the increasing amount of water are being injected through the source. The pore pressure drops when the injection pauses, but the plume is still expanding, driven by the excess pore pressure that has not been entirely diffused. When the injection is resumed, the pore pressure rises again. The presence of the fault with higher permeability disturbs the pressure plume. The fluid flows more quickly to the top surface through the channel inside the fault. As for the micropore pressure field, it has a similar but delayed evolution behavior, due to the time required for the fluid transfer between macropores and micropores. The difference between macropore and micropore
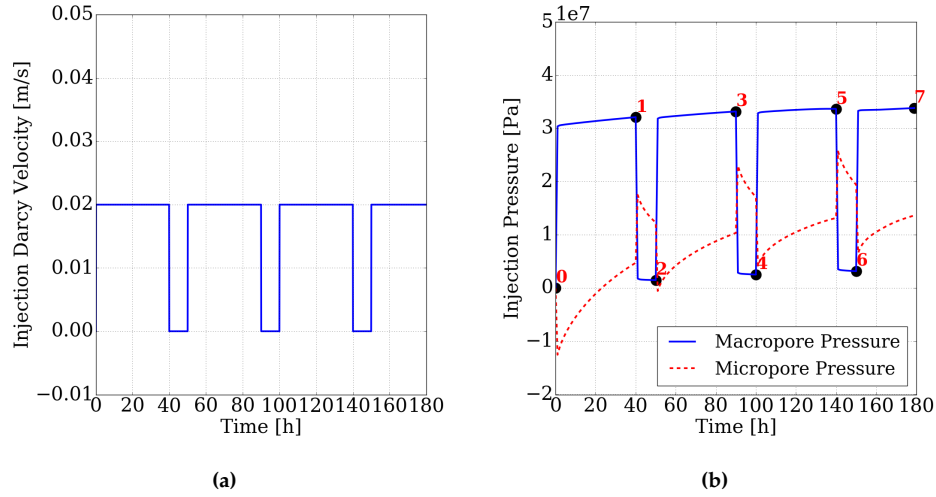
Fig. 13: Water supply in the fault reactivation problem. (a) Time history of the prescribed injection velocity in macropore at the source point. (b) Computed responses of injection pressure in macropore and micropore at the source point. The numbers mark the sequence of injection-pause cycles.

pressure is due to the different permeability in macropores and micropores for the fluid to diffuse in the macro-scale field, and also the low transfer permeability between pores.

Due to the fully coupled nature of the problem, the mechanical responses of the porous solid, especially the displacement jump and traction at the strong discontinuity, strongly depend on how pore fluid diffuses inside the pore space. The evolution of macro-scale mean effective stress field during the fluid injection cycles is shown in Fig. 15. The increase in the mean effective stress is due to the increase in excess pore pressure, in agreement to the effective stress principle Eq. 13. This results in a reduction in the normal compression traction. As the fault is frictional, this reduction in normal compression also reduce the shear strength and ultimately leads to the reactivation of the fault. The slip can be clearly observed from the changes in deviatoric strain field illustrated in 16. The deviatoric strain gradually increases and concentrates inside the fault zone. This simulation result suggests the hazardous effect of injecting water to the underground, as a fast fluid flow may trigger the slip of a nearby pre-existing fault, leading to the failure of the foundation.

The local responses to the fluid injection-pause cycles, including the spatial displacement jump, effective nominal traction and spatial macropore permeability, are illustrated in Fig. 17, Fig. 18 and 19 respectively for three locations A, B, C in the fault indicated in Fig. 16. The plots clearly illustrate the failure of the fault system by the opening and sliding of the local microstructures, caused by reductions in both normal and tangential tractions. These results demonstrate the capacity of our proposed multiscale model in capturing the complex mechanical and hydraulic behaviors of the interfacial materials. This is an improvement over the phenomenological traction-separation laws where idealized tensile and shear (linear or exponential) behavior is often adopted [Park and Paulino, 2011].

6 Conclusion

In this work, we present, for the first time, a multiscale coupling model that captures the hydro-mechanical responses of dual-permeability porous media with strong discontinuities in the finite deformation range. The traction-separation law is homogenized from DEM RVEs located in the strong discontinuity, and the interfacial permeability is given by a data-driven model trained with Lattice-Boltzmann simulations on deformed RVEs. An enhanced-strain dual-porosity formulation suitable for incorporating the homogenized constitutive laws is derived. The proposed semi-data-driven multiscale framework is capable of simulat-

(a) 40 hours   **(b)** 100 hours   **(c)** 180 hours

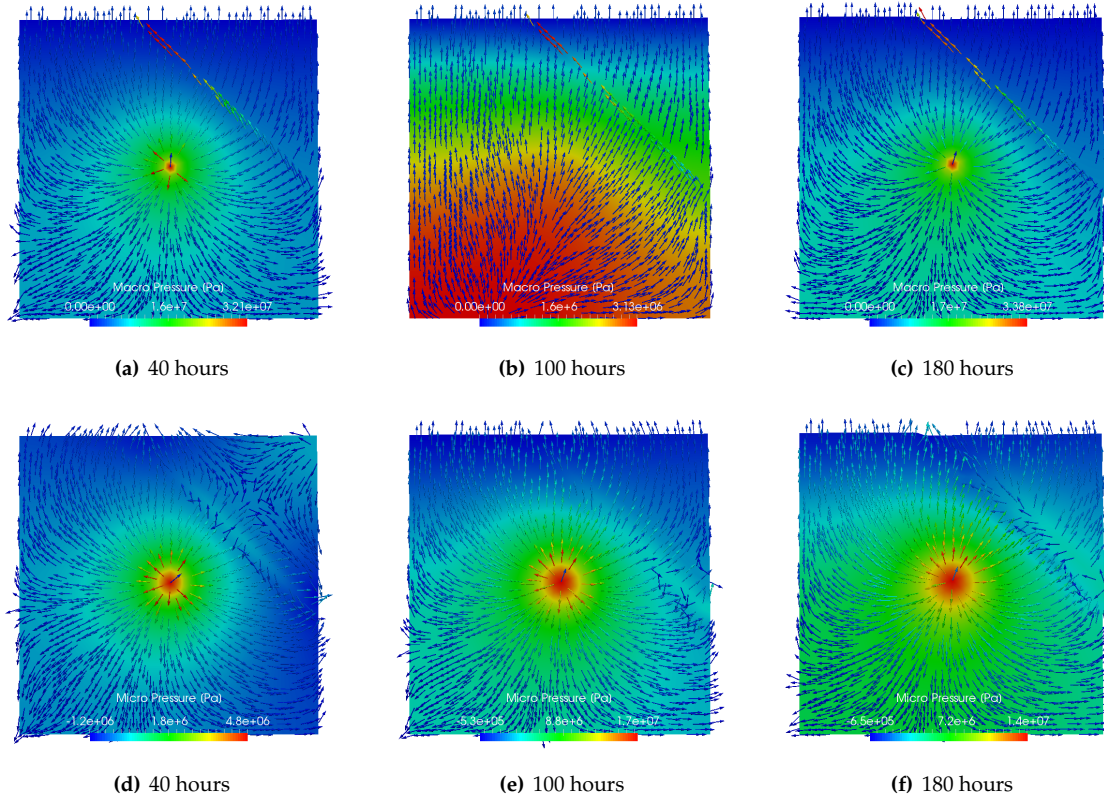**(d)** 40 hours   **(e)** 100 hours   **(f)** 180 hours

Fig. 14: Evolution of macropore pressure (a-c) and micropore pressure (d-f) field. Arrows indicate the fluid flux vector field in macropores (a-c) and in micropores (d-f). The non-zero components normal to the impervious boundaries are due to the inaccuracy of the nodal projection of the flow vector field evaluated at quadrature points.

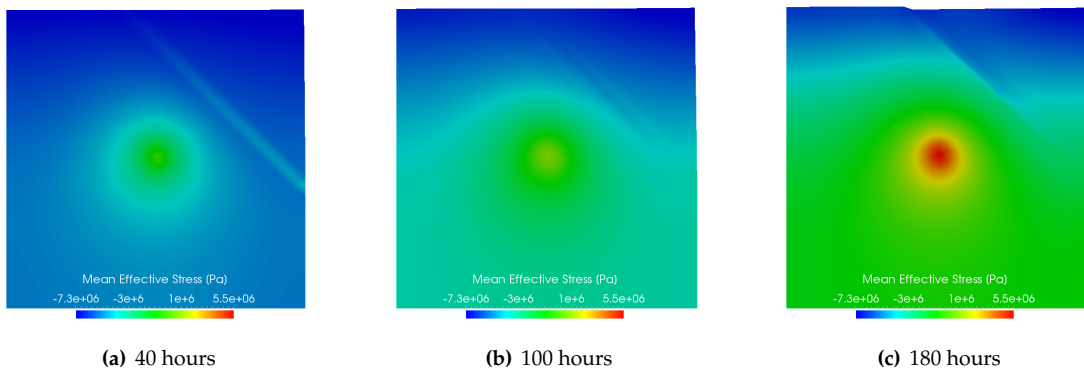**(a)** 40 hours   **(b)** 100 hours   **(c)** 180 hours

Fig. 15: Evolution of the mean effective stress field in the macro-scale simulation.

ing complex and fully coupled geomechanics problems with pre-existing and non-propagating fractures. This is demonstrated by mixed-mode shear tests that showcase the opening and shearing of interfaces and induced fluid flow in the specimen, as well as a field-scale problem that showcase the failure of a fault system induced by the underground injection of fluid.
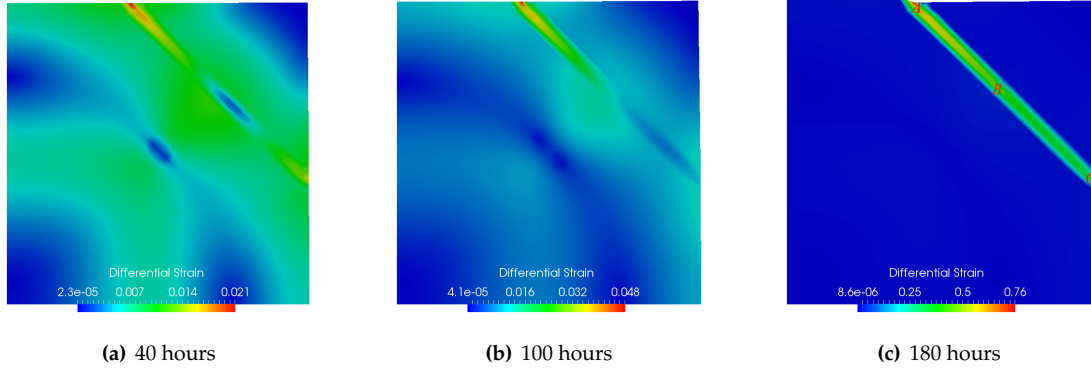
(a) 40 hours   **(b)** 100 hours   **(c)** 180 hours

Fig. 16: Evolution of the differential strain field in the macro-scale simulation.

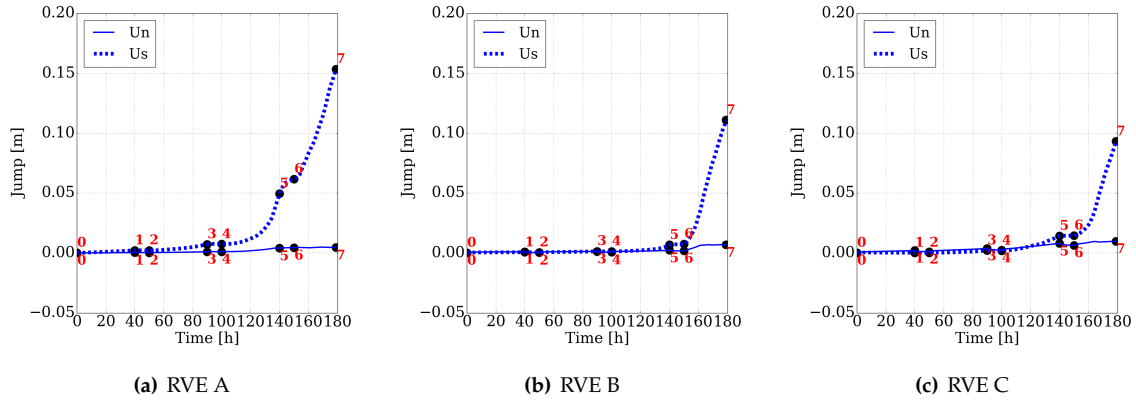**(a)** RVE A   **(b)** RVE B   **(c)** RVE C

Fig. 17: History of normal Un and tangential Us components of the displacement jump $[\![u]\!]$ for local RVEs A, B and C (location shown in Fig. 16). The numbers mark the sequence of injection-pause cycles (Fig. 13).

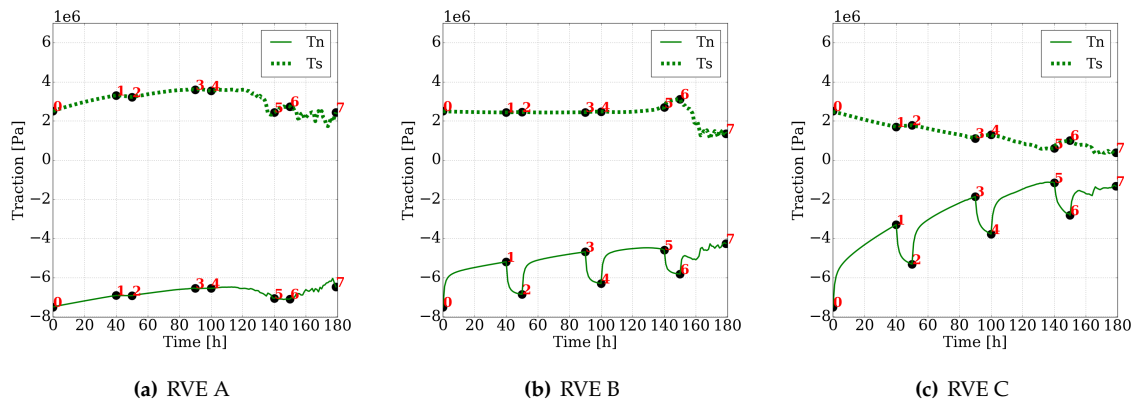**(a)** RVE A   **(b)** RVE B   **(c)** RVE C

Fig. 18: History of normal Tn and tangential Ts components of the effective nominal traction T' for local RVEs A, B and C (location shown in Fig. 16). The numbers mark the sequence of injection-pause cycles (Fig. 13).
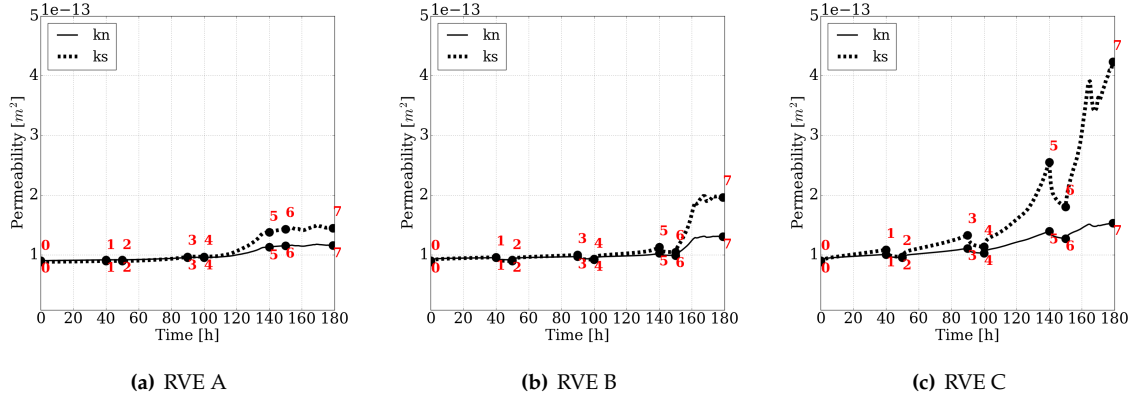
(a) RVE A   **(b)** RVE B   **(c)** RVE C

Fig. 19: History of normal kn and tangential ks components of the macropore permeability k_{RVE} for local RVEs A, B and C (location shown in Fig. 16). The numbers mark the sequence of injection-pause cycles (Fig. 13).

7 Acknowledgments

Appendix A. Consistent linearization of the finite strain double porosity formulation

Continuing the linearization of the weak form of the linear momentum conservation equation (50) after Section 4.3,

$$\delta g_3 = - \int_{\mathcal{B}} \boldsymbol{\eta} \cdot J \rho_f \left(\nabla^x \cdot \delta \boldsymbol{u} \right) \boldsymbol{g} \, dV. \tag{68}$$

$$
\begin{aligned}
\delta g_4 &= \int_{\mathcal{B}} \boldsymbol{\eta} \cdot \delta J \, c \left(\widetilde{\boldsymbol{v}}_m - \widetilde{\boldsymbol{v}}_M \right) dV + \int_{\mathcal{B}} \boldsymbol{\eta} \cdot J \, \delta c \left(\widetilde{\boldsymbol{v}}_m - \widetilde{\boldsymbol{v}}_M \right) dV + \int_{\mathcal{B}} \boldsymbol{\eta} \cdot J \, c \left(\delta \widetilde{\boldsymbol{v}}_m - \delta \widetilde{\boldsymbol{v}}_M \right) dV \\
&= \int_{\mathcal{B}} \boldsymbol{\eta} \cdot J (\nabla^x \cdot \delta \boldsymbol{u}) \, c \left(\widetilde{\boldsymbol{v}}_m - \widetilde{\boldsymbol{v}}_M \right) dV \\
&\quad + \int_{\mathcal{B}} \boldsymbol{\eta} \cdot J \, \frac{\bar{\alpha}}{\mu_f} \left(\delta p_M - \delta p_m \right) \left(\widetilde{\boldsymbol{v}}_m - \widetilde{\boldsymbol{v}}_M \right) dV + \int_{\mathcal{B}} \boldsymbol{\eta} \cdot J \, \frac{1}{\mu_f} \frac{\partial \bar{\alpha}}{\partial \boldsymbol{u}} \delta \boldsymbol{u} \left(p_M - p_m \right) \left(\widetilde{\boldsymbol{v}}_m - \widetilde{\boldsymbol{v}}_M \right) dV \\
&\quad + \int_{\mathcal{B}} \boldsymbol{\eta} \cdot J \, c \left(\delta \widetilde{\boldsymbol{v}}_m - \delta \widetilde{\boldsymbol{v}}_M \right) dV.
\end{aligned}
\tag{69}
$$

The last linearized term requires the linearization of the relative velocity of macropore

$$
\begin{aligned}
&\delta \tilde{\boldsymbol{v}}_M \\
&= \delta(\frac{\boldsymbol{q}_M}{\rho_f \phi \psi}) \\
&= \delta(\frac{-\boldsymbol{k}_M \cdot (\nabla^x p_M - \rho_f \boldsymbol{g})}{\mu_f \, \phi \, \psi}) \\
&= -\frac{1}{\mu_f} \frac{\delta[\boldsymbol{k}_M \cdot (\nabla^x p_M - \rho_f \boldsymbol{g})] \, \phi \, \psi - \boldsymbol{k}_M \cdot (\nabla^x p_M - \rho_f \boldsymbol{g}) \, \delta(\phi \, \psi)}{(\phi \, \psi)^2},
\end{aligned}
\tag{70}
$$

where

$$
\begin{aligned}
&\delta[\boldsymbol{k}_M \cdot (\nabla^x p_M - \rho_f \boldsymbol{g})] \\
&= \frac{\partial \boldsymbol{k}_M}{\partial \boldsymbol{u}} \delta \boldsymbol{u} \cdot (\nabla^x p_M - \rho_f \boldsymbol{g}) + \boldsymbol{k}_M \cdot (\nabla^x \delta p_M - \nabla^x p_M \cdot \nabla^x \delta \boldsymbol{u}),
\end{aligned}
\tag{71}
$$

and

$$
\begin{aligned}
&\delta(\phi \, \psi) \\
&= \frac{\partial \phi}{\partial \boldsymbol{u}} \delta \boldsymbol{u} \, \psi + \phi \, \frac{\partial \psi}{\partial \boldsymbol{u}} \delta \boldsymbol{u},
\end{aligned}
\tag{72}
$$

and

$$
\phi = 1 - (1 - \phi_0)\frac{1}{J}, \quad \delta\phi = (1 - \phi_0)\frac{\delta J}{J^2} = (1 - \phi_0)\frac{\nabla^x \cdot \delta \boldsymbol{u}}{J} = (1 - \phi) \, \nabla^x \cdot \delta \boldsymbol{u}.
\tag{73}
$$

The linearization of the relative velocity of micropore follows similar derivations as above.

For the linearization of the weak form of the mass conservation equation for macropore (51), using Eq. (5),

$$
\begin{aligned}
\delta h_1^M &= \int_{\mathcal{B}} \zeta_M \, \delta \rho_0^M \, dV \\
&= \int_{\mathcal{B}} \zeta_M \, J \, \rho_f \, \psi \, \nabla^x \cdot \delta \boldsymbol{u} \, dV + \int_{\mathcal{B}} \zeta_M \, J \, \rho_f \, \phi \, \frac{\partial \psi}{\partial \boldsymbol{u}} \delta \boldsymbol{u} \, dV
\end{aligned}
\tag{74}
$$

$$
\begin{aligned}
\delta h_2^M &= + \Delta t \, \rho_f \int_{\mathcal{B}} \delta(\nabla^x \zeta_M) \cdot J \, \frac{\boldsymbol{k}_M}{\mu_f} \cdot (\nabla^x p_M - \rho_f \boldsymbol{g}) \, dV + \Delta t \, \rho_f \int_{\mathcal{B}} \nabla^x \zeta_M \cdot \delta J \, \frac{\boldsymbol{k}_M}{\mu_f} \cdot (\nabla^x p_M - \rho_f \boldsymbol{g}) \, dV \\
&\quad + \Delta t \, \rho_f \int_{\mathcal{B}} \nabla^x \zeta_M \cdot J \, \frac{\delta \boldsymbol{k}_M}{\mu_f} \cdot (\nabla^x p_M - \rho_f \boldsymbol{g}) \, dV + \Delta t \, \rho_f \int_{\mathcal{B}} \nabla^x \zeta_M \cdot J \, \frac{\boldsymbol{k}_M}{\mu_f} \cdot \delta(\nabla^x p_M) \, dV \\
&= - \Delta t \, \rho_f \int_{\mathcal{B}} \nabla^x \zeta_M \cdot \nabla^x \delta \boldsymbol{u} \cdot J \, \frac{\boldsymbol{k}_M}{\mu_f} \cdot (\nabla^x p_M - \rho_f \boldsymbol{g}) \, dV \\
&\quad + \Delta t \, \rho_f \int_{\mathcal{B}} \nabla^x \zeta_M \cdot J \, (\nabla^x \cdot \delta \boldsymbol{u}) \, \frac{\boldsymbol{k}_M}{\mu_f} \cdot (\nabla^x p_M - \rho_f \boldsymbol{g}) \, dV \\
&\quad + \Delta t \, \rho_f \int_{\mathcal{B}} \nabla^x \zeta_M \cdot J \, \frac{1}{\mu_f} \frac{\partial \boldsymbol{k}_M}{\partial \boldsymbol{u}} \delta \boldsymbol{u} \cdot (\nabla^x p_M - \rho_f \boldsymbol{g}) \, dV \\
&\quad + \Delta t \, \rho_f \int_{\mathcal{B}} \nabla^x \zeta_M \cdot J \, \frac{\boldsymbol{k}_M}{\mu_f} \cdot (\nabla^x \delta p_M - \nabla^x p_M \cdot \nabla^x \delta \boldsymbol{u}) \, dV
\end{aligned}
\tag{75}
$$

$$
\begin{aligned}
\delta h_3^M &= \Delta t \int_{\mathcal{B}} \zeta_M \, \delta J \, c \, dV + \Delta t \int_{\mathcal{B}} \zeta_M \, J \, \delta c \, dV \\
&= \Delta t \int_{\mathcal{B}} \zeta_M \, J \, (\nabla^x \cdot \delta \boldsymbol{u}) \, c \, dV + \Delta t \int_{\mathcal{B}} \zeta_M \, J \, \frac{\bar{\alpha}}{\mu_f} (\delta p_M - \delta p_m) \, dV + \Delta t \int_{\mathcal{B}} \zeta_M \, J \, \frac{1}{\mu_f} \frac{\partial \bar{\alpha}}{\partial \boldsymbol{u}} \delta \boldsymbol{u} \, (p_M - p_m) \, dV
\end{aligned}
\tag{76}
$$

The linearization of the weak form of the mass conservation equation for micropore (52) follows similar derivations as above.

References

Todd Arbogast, Jim Douglas, Jr, and Ulrich Hornung. Derivation of the double porosity model of single phase flow via homogenization theory. *SIAM Journal on Mathematical Analysis*, 21(4):823–836, 1990.

Francisco Armero. Large-scale modeling of localized dissipative mechanisms in a local continuum: applications to the numerical simulation of strain localization in rate-dependent inelastic solids. *Mechanics of Cohesive-frictional Materials*, 4(2):101–131, 1999.

Francisco Armero and Carlo Callari. An analysis of strong discontinuities in a saturated poro-plastic solid. *International journal for numerical methods in engineering*, 46(10):1673–1698, 1999.

Francisco Armero and Krishna Garikipati. An analysis of strong discontinuities in multiplicative finite strain plasticity and their relation with the numerical simulation of strain localization in solids. *International Journal of Solids and Structures*, 33(20-22):2863–2885, 1996.

Francisco Armero and Christian Linder. New finite elements with embedded strong discontinuities in the finite deformation range. *Computer Methods in Applied Mechanics and Engineering*, 197(33-40):3138–3170, 2008.

Ted Belytschko, Wing Kam Liu, Brian Moran, and Khalil Elkhodary. *Nonlinear finite elements for continua and structures*. John wiley & sons, 2013.

Joseph E Bishop. Simulating the pervasive fracture of materials and structures using randomly close packed voronoi tessellations. *Computational Mechanics*, 44(4):455–471, 2009.

Ronaldo I Borja. Finite element simulation of strain localization with large deformation: capturing strong discontinuity using a petrov–galerkin multiscale formulation. *Computer Methods in Applied Mechanics and Engineering*, 191(27):2949–2978, 2002.

Ronaldo I Borja. Assumed enhanced strain and the extended finite element methods: A unification of concepts. *Computer Methods in Applied Mechanics and Engineering*, 197(33):2789–2803, 2008.

Ronaldo I Borja and Jinhyun Choo. Cam-clay plasticity, part viii: A constitutive framework for porous materials with evolving internal structure. *Computer Methods in Applied Mechanics and Engineering*, 309: 653–679, 2016.

Emanuela Bosco, VG Kouznetsova, EWC Coenen, MGD Geers, and Alberto Salvadori. A multiscale framework for localizing microstructures towards the onset of macroscopic discontinuity. *Computational Mechanics*, 54(2):299–319, 2014.

Carlo Callari and Francisco Armero. Finite element methods for the analysis of strong discontinuities in coupled poro-plastic media. *Computer Methods in Applied Mechanics and Engineering*, 191(39-40):4371–4400, 2002.

Carlo Callari and Francisco Armero. Analysis and numerical simulation of strong discontinuities in finite strain poroplasticity. *Computer Methods in Applied Mechanics and Engineering*, 193(27-29):2941–2986, 2004.

Carlo Callari and F Federico. Fem validation of a double porosity elastic model for consolidation of structurally complex clayey soils. *International journal for numerical and analytical methods in geomechanics*, 24 (4):367–402, 2000.

Jinhyun Choo and Ronaldo I Borja. Stabilized mixed finite elements for deformable porous media with double porosity. *Computer Methods in Applied Mechanics and Engineering*, 293:131–154, 2015.

Jinhyun Choo, Joshua A White, and Ronaldo I Borja. Hydromechanical modeling of unsaturated flow in double porosity media. *International Journal of Geomechanics*, page D4016002, 2016.

E WC Coenen, VG Kouznetsova, E Bosco, and M GD Geers. A multi-scale approach to bridge microscale damage and macroscale failure: a nested computational homogenization-localization framework. *International Journal of Fracture*, pages 1–22, 2012.

René de Borst. Fluid flow in fractured and fracturing porous media: A unified view. *Mechanics Research Communications*, 2016.

René de Borst. A classification of poromechanical interface elements. *Journal of Modeling in Mechanics and Materials*, 1(1), 2017a.

René de Borst. Fluid flow in fractured and fracturing porous media: A unified view. *Mechanics Research Communications*, 80:47–57, 2017b.

René De Borst, Mike A Crisfield, Joris JC Remmers, and Clemens V Verhoosel. *Nonlinear finite element analysis of solids and structures*. John Wiley & Sons, 2012.

Wim Degruyter, Alain Burgisser, Olivier Bachmann, and Orestis Malaspinas. Synchrotron x-ray micro-tomography and lattice boltzmann simulations of gas flow through volcanic pumices. *Geosphere*, 6(5): 470–481, 2010.

John Dolbow and Ted Belytschko. A finite element method for crack growth without remeshing. *International journal for numerical methods in engineering*, 46(1):131–150, 1999.

X Du and M Ostoja-Starzewski. On the size of representative volume element for darcy law in random media. In *Proceedings of the Royal Society of London A: Mathematical, Physical and Engineering Sciences*, volume 462, pages 2949–2963. The Royal Society, 2006.

Usama El Shamy and Yasser Abdelhamid. Modeling granular soils liquefaction using coupled lattice boltzmann method and discrete element method. *Soil Dynamics and Earthquake Engineering*, 67:119–132, 2014.

SA Galindo-Torres, A Scheuermann, HB Mühlhaus, and DJ Williams. A micro-mechanical approach for the study of contact erosion. *Acta Geotechnica*, 10(3):357–368, 2015.

HH Gerke and MT Van Genuchten. A dual-porosity model for simulating the preferential movement of water and solutes in structured porous media. *Water resources research*, 29(2):305–319, 1993.

Jamshid Ghaboussi, David A Pecknold, Mingfu Zhang, and Rami M Haj-Ali. Autoprogressive training of neural network constitutive models. *International Journal for Numerical Methods in Engineering*, 42(1): 105–126, 1998.

Bin Gong, Mohammad Karimi-Fard, Louis J Durlofsky, et al. Upscaling discrete fracture characterizations to dual-porosity, dual-permeability models for efficient simulation of flow with strong gravitational effects. *SPE Journal*, 13(01):58–67, 2008.

Yonggui Guo and Julia K Morgan. Fault gouge evolution and its dependence on normal stress and rock strength—results of discrete element simulations: Gouge zone properties. *Journal of Geophysical Research: Solid Earth*, 112(B10), 2007.

CB Hirschberger, S Ricker, P Steinmann, and N Sukumar. Computational multiscale modelling of heterogeneous material layers. *Engineering Fracture Mechanics*, 76(6):793–812, 2009.

Claudia Britta Hirschberger, Natarajan Sukumar, and Paul Steinmann. Computational homogenization of material layers with micromorphic mesostructure. *Philosophical Magazine*, 88(30-32):3603–3631, 2008.

Sepp Hochreiter and Jürgen Schmidhuber. Long short-term memory. *Neural computation*, 9(8):1735–1780, 1997.

J Kim, HA Tchelepi, and R Juanes. Stability and convergence of sequential methods for coupled flow and geomechanics: Fixed-stress and fixed-strain splits. *Computer Methods in Applied Mechanics and Engineering*, 200(13):1591–1606, 2011.

Kristopher L Kuhlman, Bwalya Malama, and Jason E Heath. Multiporosity flow in fractured low-permeability rocks. *Water Resources Research*, 51(2):848–860, 2015.

Matthew R Kuhn, WaiChing Sun, and Qi Wang. Stress-induced anisotropy in granular materials: fabric, stiffness, and permeability. *Acta Geotechnica*, 10(4):399–419, 2015.

Jonas Larsson and Ragnar Larsson. Finite-element analysis of localization of deformation and fluid pressure in an elastoplastic porous medium. *International journal of solids and structures*, 37(48):7231–7257, 2000.

Edouard Le Garzic, Thibaut de L'Hamaide, Marc Diraison, Yves Géraud, Judith Sausse, Marc De Urreiztieta, Benoît Hauville, and Jean-Michel Champanhet. Scaling and geometric properties of extensional fracture systems in the proterozoic basement of yemen. tectonic interpretation and fluid flow implications. *Journal of Structural Geology*, 33(4):519–536, 2011.

M Lefik and BA Schrefler. Artificial neural network for parameter identifications for an elasto-plastic model of superconducting cable under cyclic loading. *Computers & structures*, 80(22):1699–1713, 2002.

Jolanta Lewandowska, Adam Szymkiewicz, Kazimierz Burzyński, and Michel Vauclin. Modeling of unsaturated water flow in double-porosity soils by the homogenization approach. *Advances in Water Resources*, 27(3):283–296, 2004.

Fushen Liu and Ronaldo I Borja. A contact algorithm for frictional crack propagation with the extended finite element method. *International Journal for Numerical methods in engineering*, 76(10):1489–1512, 2008.

Yang Liu, WaiChing Sun, Zifeng Yuan, and Jacob Fish. A nonlocal multiscale discrete-continuum model for predicting mechanical behavior of granular materials. *International Journal for Numerical Methods in Engineering*, 2015.

C Miehe, J Dettmar, and D Zäh. Homogenization and two-scale simulations of granular materials for different microstructural constraints. *International Journal for Numerical Methods in Engineering*, 83(8-9): 1206–1236, 2010.

Christian Miehe and Joachim Dettmar. A framework for micro–macro transitions in periodic particle aggregates of granular materials. *Computer Methods in Applied Mechanics and Engineering*, 193(3):225–256, 2004.

Andro Mikelić and Mary F Wheeler. Convergence of iterative coupling for coupled flow and geomechanics. *Computational Geosciences*, 17(3):455–461, 2013.

Nicolas Moës, John Dolbow, and Ted Belytschko. A finite element method for crack growth without remeshing. *Int. J. Numer. Meth. Engng*, 46:131–150, 1999.

T Mohammadnejad and AR Khoei. An extended finite element method for hydraulic fracture propagation in deformable porous media with the cohesive crack model. *Finite Elements in Analysis and Design*, 73: 77–95, 2013.

J Mosler. Modeling strong discontinuities at finite strains—a novel numerical implementation. *Computer Methods in Applied Mechanics and Engineering*, 195(33):4396–4419, 2006.

Mijo Nikolic, Adnan Ibrahimbegovic, and Predrag Miscevic. Modelling of internal fluid flow in cracks with embedded strong discontinuities. In *Computational Methods for Solids and Fluids*, pages 315–341. Springer, 2016.

J Oliver, M Caicedo, Emmanuel Roubin, Alfredo Edmundo Huespe, and JA Hernández. Continuum approach to computational multiscale modeling of propagating fracture. *Computer Methods in Applied Mechanics and Engineering*, 294:384–427, 2015.

Martin Ostoja-Starzewski, X Du, ZF Khisaeva, and W Li. Comparisons of the size of the representative volume element in elastic, plastic, thermoelastic, and permeable random microstructures. *International Journal for Multiscale Computational Engineering*, 5(2), 2007.

A Pandolfi, PR Guduru, M Ortiz, and AJ Rosakis. Three dimensional cohesive-element analysis and experiments of dynamic fracture in c300 steel. *International Journal of Solids and Structures*, 37(27):3733–3760, 2000.

Kyoungsoo Park and Glaucio H Paulino. Cohesive zone models: a critical review of traction-separation relationships across fracture surfaces. *Applied Mechanics Reviews*, 64(6):060802, 2011.

Mervyn S Paterson and Teng-fong Wong. *Experimental rock deformation-the brittle field*. Springer Science & Business Media, 2005.

Jean H Prevost and N Sukumar. Faults simulations for three-dimensional reservoir-geomechanical models with the extended finite element method. *Journal of the Mechanics and Physics of Solids*, 86:1–18, 2016.

Steven R Pride and James G Berryman. Linear dynamics of double-porosity dual-permeability materials. i. governing equations and acoustic attenuation. *Physical Review E*, 68(3):036603, 2003.

Raúl Radovitzky, Andrew Seagraves, Mike Tupek, and Ludovic Noels. A scalable 3d fracture and fragmentation algorithm based on a hybrid, discontinuous galerkin, cohesive element method. *Computer Methods in Applied Mechanics and Engineering*, 200(1):326–344, 2011.

Andrea Francesco Rotunno, Carlo Callari, and Francesco Froiio. Computational modeling of backward erosion piping. In *Models, Simulation, and Experimental Issues in Structural Mechanics*, pages 225–234. Springer, 2017.

LUC Scholtès and Frédéric-Victor Donzé. Modelling progressive failure in fractured rock masses using a 3d discrete element method. *International Journal of Rock Mechanics and Mining Sciences*, 52:18–30, 2012.

Luc Scholtès and Frédéric-Victor Donzé. A dem model for soft and hard rocks: role of grain interlocking on strength. *Journal of the Mechanics and Physics of Solids*, 61(2):352–369, 2013.

Xiaoyu Song and Ronaldo I Borja. Mathematical framework for unsaturated flow in the finite deformation range. *International Journal for Numerical Methods in Engineering*, 97(9):658–682, 2014.

P Steinmann. A finite element formulation for strong discontinuities in fluid-saturated porous media. *Mechanics of Cohesive-frictional Materials*, 4(2):133–152, 1999.

WaiChing Sun, Jose E Andrade, and John W Rudnicki. Multiscale method for characterization of porous microstructures and their impact on macroscopic effective permeability. *International Journal for Numerical Methods in Engineering*, 88(12):1260–1279, 2011a.

WaiChing Sun, José E Andrade, John W Rudnicki, and Peter Eichhubl. Connecting microstructural attributes and permeability from 3d tomographic images of in situ shear-enhanced compaction bands

using multiscale computations. *Geophysical Research Letters*, 38(10), 2011b.

WaiChing Sun, Matthew R Kuhn, and John W Rudnicki. A multiscale dem-lbm analysis on permeability evolutions inside a dilatant shear band. *Acta Geotechnica*, 8(5):465–480, 2013.

WaiChing Sun, Zhijun Cai, and Jinhyun Choo. Mixed arlequin method for multiscale poromechanics problems. *International Journal for Numerical Methods in Engineering*, 2016.

Sebastian Toro, Pablo J Sánchez, Alfredo Edmundo Huespe, Sebastian Miguel Giusti, Pedro J Blanco, and RA Feijóo. A two-scale failure model for heterogeneous materials: numerical implementation based on the finite element method. *International Journal for Numerical Methods in Engineering*, 97(5):313–351, 2014.

Sebastian Toro, PJ Sánchez, JM Podestá, PJ Blanco, Alfredo Edmundo Huespe, and RA Feijóo. Cohesive surface model for fracture based on a two-scale formulation: computational implementation aspects. *Computational mechanics*, 58(4):549–585, 2016.

DK Tran, N Prime, F Froiio, Carlo Callari, and E Vincens. Numerical modelling of backward front propagation in piping erosion by dem-lbm coupling. *European Journal of Environmental and Civil Engineering*, 21(7-8):960–987, 2017.

Viggo Tvergaard and John W Hutchinson. The relation between crack growth resistance and fracture process parameters in elastic-plastic solids. *Journal of the Mechanics and Physics of Solids*, 40(6):1377–1397, 1992.

I Vardoulakis. Deformation of water-saturated sand: I. uniform undrained deformation and shear banding. *Géotechnique*, 46(3):441–456, 1996.

V. Šmilauer and B. Chareyre. Dem formulation. In *Yade Documentation 2nd ed*. The Yade Project, 2015. doi: 10.5281/zenodo.34044. http://yade-dem.org/doc/.

Kun Wang and WaiChing Sun. A semi-implicit discrete-continuum coupling method for porous media based on the effective stress principle at finite strain. *Computer Methods in Applied Mechanics and Engineering*, 304:546 – 583, 2016a. ISSN 0045-7825.

Kun Wang and Waiching Sun. A semi-implicit micropolar discrete-to-continuum method for granular materials. In M Papadrakakis, V Papadopoulos, G Stefanou, and V Plevris, editors, *Proceedings of European Congress on Computational Methods in Applied Science and Engineering*, number June, pages 5–10, Crete Island, 2016b.

Kun Wang and WaiChing Sun. Data-driven discrete-continuum method for partially saturated micro-polar porous media. In *Poromechanics VI*, pages 571–578. 2017a.

Kun Wang and WaiChing Sun. A unified variational eigen-erosion framework for interacting brittle fractures and compaction bands in fluid-infiltrating porous media. *Computer Methods in Applied Mechanics and Engineering*, 318:1–32, 2017b.

Kun Wang and WaiChing Sun. A multiscale multi-permeability poroplasticity model linked by recursive homogenizations and deep learning. *Computer Methods in Applied Mechanics and Engineering*, 334:337–380, 2018.

Christopher AJ Wibberley, Jamil Gonzalez-Dunia, and Olivier Billon. Faults as barriers or channels to production-related flow: insights from case studies. *Petroleum Geoscience*, pages petgeo2016–057, 2016.

Ines Wollny, WaiChing Sun, and Michael Kaliske. A hierarchical sequential ale poromechanics model for tire-soil-water interaction on fluid-infiltrated roads. *International Journal for Numerical Methods in Engineering*, 2017.

X-P Xu and Alan Needleman. Numerical simulations of fast crack growth in brittle solids. *Journal of the Mechanics and Physics of Solids*, 42(9):1397–1434, 1994.